Atmospheric
Measurement
Techniques
Discussions

Open Access

A generalized method for discriminating thermodynamic phase and retrieving cloud optical thickness and effective radius using transmitted shortwave radiance spectra

S. E. LeBlanc[1,2,*], P. Pilewskie[1,2], K. S. Schmidt[2], and O. Coddington[2]

[1]University of Colorado, Department of Atmospheric and Oceanic Sciences, Boulder, Colorado, USA
[2]University of Colorado, Laboratory for Atmospheric and Space Physics, Boulder, Colorado, USA
[*]now at: NASA Ames Research Center, Moffett Field, California, USA

Correspondence to: S. E. LeBlanc (samuel.leblanc@nasa.gov)

Abstract

A new retrieval scheme for cloud optical thickness, effective radius, and thermodynamic phase was developed for ground-based measurements of cloud shortwave spectral transmittance. 15 parameters were derived to quantify spectral variations in shortwave
5 transmittance due to absorption and scattering of liquid water and ice clouds, manifested by shifts in spectral slopes, curvatures, maxima, and minima. To retrieve cloud optical thickness and effective particle radius a weighted least square fit that matched the modeled parameters was applied. The measurements for this analysis were made with a ground-based Solar Spectral Flux Radiometer (SSFR) in Boulder, Colorado,
10 between May 2012 and January 2013. We compared the cloud optical thickness and effective radius from the new retrieval to two other retrieval methods. By using multiple spectral features, we find a closer fit (with a root mean square difference over the entire spectra of 3.1 % for a liquid water cloud and 5.9 % for an ice cloud) between measured and modeled spectra compared to two other retrieval methods, which diverge by a root-
15 mean-square of up to 6.4 % for a liquid water cloud and 22.5 % for an ice cloud. The new retrieval introduced here has an average uncertainty in effective radius ($\pm 1.2\,\mu m$) smaller by factor of at least 2.5 than two other methods when applied to an ice cloud.

1 Introduction

Clouds strongly influence Earth's radiative energy balance by modulating the trans-
20 fer of shortwave radiation through the atmosphere. Clouds reduce the globally averaged solar radiation absorbed at the surface by $53\,W\,m^{-2}$ and produce a net cooling of $21\,W\,m^{-2}$ (Allan, 2011). Cloud radiative effects are governed by optical thickness (τ), cloud particle effective radius (r_e) and thermodynamic phase (ϕ) (see, for example, Key and Intrieri, 2000; Sun and Shine, 1995; Wiscombe et al., 1984). Droplet size and
25 water phase influences single-scattering and absorption, primarily in the near-infrared region (Slingo, 1990; Twomey and Bohren, 1980; Wiscombe et al., 1984). For example,

a liquid water droplet scatters more strongly in the forward direction than an ice parti-cle of equivalent size (e.g., Baum et al., 2011). Furthermore, differences in bulk liquid water and ice absorption in the near infrared (between 700–2500 nm) have observable consequences in cloud spectral reflectance and transmittance that can be exploited to retrieve cloud thermodynamic phase (e.g., Pilewskie and Twomey, 1987).

In the shortwave spectral region, optical thickness, particle size, and thermodynamic phase are most often retrieved using reflectance measurements (e.g., Nakajima and King, 1990; Platnick et al., 2001; Twomey and Cocks, 1989). Radiation reflected at cloud top has been scattered by particles in the uppermost regions of clouds, unlike transmitted radiation which has interacted with particles throughout the entire cloud layer. For this reason, transmittance based retrievals are more representative of layer-average properties (Platnick, 2000) than their reflectance-based counterparts.

Uncertainties in retrieved cloud optical thickness and effective radius from transmit-tance are often much larger than from reflectance, particularly for thin clouds (Turner et al., 2007). Large uncertainties arise in transmittance retrievals because the informa-tion content from inverse methods optimized for reflectance is reduced when applied to cloud transmittance, particularly for particle size. This demands new methods of extracting information based on the unique physics of cloud transmittance, which is re-vealed in the observed spectral signatures. Another problem with transmittance-based retrievals is that optical thickness is not uniquely defined for all given transmittance, requiring additional information to retrieve optical thickness.

These problems have motivated the development of novel retrieval approaches spe-cific to cloud transmittance. Such approaches include: the transmittance at two wave-lengths for a cloud overlying a vegetated surface (Chiu et al., 2010; Marshak et al., 2004), the transmittance at two wavelengths where condensed water absorption varies (Kikuchi et al., 2006; Rawlins and Foot, 1990), differential optical absorption spec-troscopy (DOAS) (Daniel, 2002; Daniel et al., 2003, 2006; Schofield et al., 2007), and the slope of transmittance in selected spectral bands (McBride et al., 2012, 2011). Each of these methods has limitations. For example, using transmittance at wavelengths of

differing condensed water absorption (Kikuchi et al., 2006; Rawlins and Foot, 1990) results in non-unique solutions of τ and r_e at optical thicknesses below 10 and large uncertainties in r_e at larger optical thicknesses. DOAS requires either assumptions or measurements of the photon path length to retrieve τ, r_e, and ϕ. The method described

5 by McBride et al. (2011) has higher sensitivity to effective radius than others, yet it is susceptible to systematic biases in absolute radiometric calibration and surface albedo (Coddington et al., 2013) and has thus far been applied to liquid clouds only.

The current work introduces 15 parameters that quantify several spectral features of normalized cloud-transmitted radiance that are sensitive to τ, r_e, and ϕ. This work is

10 motivated by McBride et al. (2011) who derived one parameter, the spectral slope of transmittance between 1565–1637 nm to retrieved liquid cloud τ and r_e. In this work, a general method is derived that incorporates characteristics of the transmittance spectra that have not been previously exploited in a retrieval scheme. Furthermore, the sensitivity to calibration biases is reduced by utilizing normalized radiance. To find the

15 most likely combination of τ, r_e, and ϕ, we implement a two-step least squares fit of measured parameters to modeled parameters. Thermodynamic phase is retrieved first, followed by τ and r_e. A quantitative analysis of the retrieval scheme using the GEneralized Nonlinear Retrieval Analysis (GENRA, Vukicevic et al., 2010) is presented in future work.

20 Section 2 details the instrumentation and measurements used in this work. Case studies are presented in Sect. 3, followed by the radiative transfer model, the variance in radiance spectra due to changes in optical thickness, effective radius, and thermodynamic phase, and the 15 spectral parameters in Sect. 4. In Sect. 5, we introduce the retrieval and analysis methods, and apply the retrieval to measured radiance spectra

25 and compare the results to other retrieval methods. Section 6 summarizes this work and presents its important conclusions.

Title Page

Abstract | Introduction

Conclusions | References

Tables | Figures

|◀ | ▶|

◀ | ▶

Back | Close

Full Screen / Esc

Printer-friendly Version

Interactive Discussion

2 Instrumentation and measurements

Measurements of the spectral signatures of shortwave cloud transmittance were taken with the Solar Spectral Flux Radiometer (McBride et al., 2011; Pilewskie et al., 2003). The SSFR is typically used to measure upwelling and downwelling spectral irradiance onboard airborne research platforms (e.g., Kindel et al., 2010; LeBlanc et al., 2012). In this study, the SSFR was deployed with a suite of instruments on a rooftop observatory (Skywatch, http://skywatch.colorado.edu/) located above the Duane Physical Laboratory at the University of Colorado, Boulder (see Sect. 2.2).

2.1 Solar spectral flux radiometer

The ground-based SSFR used in this study has a spectral resolution of 8–12 nm and covers the wavelength range between 350–1700 nm (McBride et al., 2011). SSFR has two light collectors: one for measuring spectral downwelling irradiance and the other, spectral zenith radiance. The radiance light collector is composed of a collimating lens with a set of baffles to restrict stray light from outside the narrow field-of-view of 2.8°. Stray light rejection was determined by rotating the light collector with respect to a collimated stable light source at 50 cm. Stray light was rejected by a factor of 10^{-5}, below the noise floor of the SSFR (0.1–0.2 %, Pilewskie et al., 2003). The radiance calibration was performed with a NIST-traceable lamp illuminating a flat Spectralon panel of known reflectance. The flat panel was viewed with the radiance light collector at 45° from normal to the panel.

The accuracy of SSFR, determined using a NIST-traceable lamp, is 3–5 % over the spectral range of SSFR. The SSFR was calibrated three times over the course of the multi-month measurement period. A change of 8 % was observed in successive absolute radiometric calibrations. Because of the large time gap between calibrations, rather than correct the data using updated calibrations which would have additional uncertainties due to interpolation error, we estimated absolute accuracy to be 8 %, the conservative upper limit based upon the spread in calibration curves. The spectrum-to-spectrum

average variation, or precision, was much better, at $0.01\,\mathrm{W\,m^{-2}\,nm^{-1}\,sr^{-1}}$ (0.2 %) for a midvisible wavelength (near 500 nm), determined by the standard deviation of measurements from a stable light source.

When a radiance spectrum is normalized by its maximum value (found to always lie between 451 nm to 490 nm) or by its value at 1000 nm, accuracy depends on wavelength-to-wavelength stability of the sensor. This stability is evaluated by the relative change of each wavelength in the 3 radiometric calibrations. The mean variation between radiance evaluated at each wavelength and the maximum radiance was 4.6 % (or 1.1 % for normalizing by the radiance at 1000 nm). This represents less variation throughout the measurement period than the absolute radiometric accuracy. Finally, the instrument was spectrally calibrated by measuring the output from a HeNe laser, Hg lamp, and a Near-IR laser diode.

2.2 Skywatch observatory

The Skywatch Observatory (http://skywatch.colorado.edu/) hosts a number of instruments for measuring atmospheric radiation and precipitation. The instruments that provided data for this study were: pyranometer, pyrgeometer, ceilometer, micro rain radar (MRR), sky webcam, and a spectral sunphotometer. The pyranometer and pyrgeometer measured broad band downwelling irradiance in the wavelength ranges of 300 to 2800 nm and 4500 to 42 000 nm respectively. The ceilometer returns cloud base height by using a pulse diode laser lidar system at 910 nm. The MRR is a K-band (24 GHz) vertical profiler of hydrometeors. The sunphotometer is a spectrometer system that tracks the sun and measures direct sunlight in the wavelength range of 350–1050 nm. These calibrated instruments provided ancillary measurements for estimating the cloud thermodynamic phase and evaluating the cloud homogeneity during SSFR measurement periods.

Title Page

Abstract | Introduction

Conclusions | References

Tables | Figures

Back | Close

Full Screen / Esc

Printer-friendly Version

Interactive Discussion

Full Screen / Esc

Printer-friendly Version

Interactive Discussion

2.3 Satellite measurements

Coincident cloud observations were made with the Geostationary Operational Environmental Satellite (GOES, Minnis et al., 1995) and the Moderate Resolution Imaging Spectroradiometer (MODIS, Platnick et al., 2003). For selected cases studied in this work, cloud top height from GOES was available for the days 25 May 2012 and 6 August 2012. MODIS derived cloud top height, cloud optical thickness, and effective radius were available on 10 January 2013. We used the MODIS 16 day averages of surface albedo (Schaaf et al., 2002) for determining the surface albedo used in the radiative transfer modeling.

3 Case studies

The SSFR was deployed at Skywatch from May 2012 to February 2013. From the collected dataset, 3 cases were selected for further study based on criteria of (i) cloud horizontal homogeneity and (ii) variations in thermodynamic phase: liquid cloud (25 May 2012), mixed phase cloud (6 August 2012), and ice cloud (10 January 2013). In this section, we describe the ancillary data used to identify the case studies.

Cloud horizontal homogeneity is required for validity of the plane-parallel assumption in the forward-model. We determined horizontal homogeneity by small temporal variability in cloud base height (measured from the ceilometer) and broadband downwelling irradiance (measured with the pyranometer for shortwave and pyrgeometer for longwave). Visual inspection of time lapse movies, captured with a sky webcam over the selected time periods, was also used to filter for heterogeneous cloud cases. An example of data taken under heterogeneous and homogeneous cloud scenes is shown in Fig. 1. In this example, the heterogeneous case has variability in shortwave irradiance of more than $800\,\mathrm{W\,m^{-2}}$ over 10 min, $40\,\mathrm{W\,m^{-2}}$ in longwave irradiance over 20 min, and cloud base heights varying from 0 (clear sky) to 6 km. By contrast, the homogeneous cloud case has little variability in short- (less than $200\,\mathrm{W\,m^{-2}}$ over a 4 h period) and

long-wave irradiance (less than $20\,\mathrm{W\,m^{-2}}$ over a 4 h period), and cloud base heights near 2 km, varying by less than 1 km.

The cloud thermodynamic phase was estimated using MRR, the ceilometer, atmospheric soundings, GOES, MODIS, and SSFR measurements of spectral radiance.
5 The atmospheric soundings for the 3 different time periods are presented in Fig. 2. Cloud base height is retrieved using the ceilometer located at the Skywatch facility for the time of interest. The cloud top height was obtained from GOES for 25 May 2012 and 6 August 2012, and from MODIS for 10 January 2013. The GOES cloud top height for 25 May 2012 was below the freezing level obtained from the atmospheric sounding.
10 Therefore, we assume that the cloud on 25 May 2012 was composed entirely of liquid water. The mixed phase case, 6 August 2012, and the ice case, 10 January 2013, had cloud base heights above the freezing level. On 6 August 2012, MRR measurements of backscatter indicated the presence of a melting layer that was also present 1 h prior to the selected case study period. In addition, GOES-retrieved cloud thermodynamic
15 phase (Minnis et al., 1995), at cloud top, was ice 15 min prior to the measurement period, and liquid during the measurement period. Therefore, we assume that the cloud on 6 August 2012 was likely mixed-phase, for this context meaning that both ice and liquid cloud particles influenced the transmitted radiation. On 10 January 2013 cloud base height was higher than 9.4 km above sea level (ASL), higher than the upper limit
20 of the ceilometer measurement. During the measurement period on 10 January 2013, MODIS cloud phase was determined to be ice. SSFR measurements of zenith transmittance showed a sharp decrease in spectral radiance near 1000 nm and 1200 nm (not shown), representative of ice absorption features (Pilewski and Twomey, 1987). Therefore, we assume that the cloud on 10 January 2013 was an ice cloud.

Title Page

Abstract   Introduction

Conclusions   References

Tables   Figures

◄   ►

◄   ►

Back   Close

Full Screen / Esc

Printer-friendly Version

Interactive Discussion

4 Radiative transfer simulations and description of retrieval parameters

4.1 Radiative transfer model

The radiative transfer model used in this study is the N-stream DISORT 2.0 (Stamnes et al., 2000) with SBDART (Ricchiazzi et al., 1998) for atmospheric molecular absorption; both are publicly available within LibRadtran (Mayer and Kylling, 2005). We varied optical thickness from 1 to 100 in increments of 1 to 10, thermodynamic phase, and effective radius from 2.5 μm to 30 μm in 2.5 μm increments for liquid drops and from 10 μm to 60 μm in 2.5 μm increments for ice particles. For liquid water clouds, Mie scattering calculations were used to obtain the scattering phase function and single scattering albedo of the cloud droplets (Evans, 1998; Wiscombe, 1980). A Gamma distribution with $\alpha = 7$, typical for liquid clouds (Mayer and Kylling, 2005), was used to represent the size distribution of the cloud droplets for each value of effective radius. For ice crystals, we used the scattering models for severely roughened general habit mixture described by Baum et al. (2011). The scattering phase function was represented by a set of 256 Legendre coefficients calculated using the method by Hu et al. (2000). We used 28 streams in DISORT 2.0 to model the spectral zenith radiance. The use of more Legendre coefficients than streams is accomplished by the truncation approximation developed by Nakajima and Tanaka (1988), which is incorporated in DISORT 2.0. The extraterrestrial solar spectral irradiance was taken from Kurucz (1994) at 1 nm spectral resolution and convolved to the slit function and spectral resolution of the SSFR.

4.2 Ancillary inputs

Spectral radiance transmitted through clouds was modeled using a set of ancillary inputs given by a prescribed spectral surface albedo, cloud base altitude, cloud extent, and atmospheric state. The atmospheric state is defined by the profiles of number concentration of atmospheric gases, pressure, temperature, and water vapor calculated from soundings taken at the Denver airport for each day of interest (see Fig. 2). Even

though τ, r_e, and ϕ control most of the variance in radiance, these sets of ancillary inputs impact the spectral radiance through multiple reflections of the below-cloud radiation.

The accuracy and precision of the retrieved cloud properties depend on an accurate knowledge of the surface albedo and atmospheric state for each measurement period. By choosing conditions that occurred for each day during the measurement, we seek to reduce this source of error. Of the 3 days selected for case study, 2 days were in the spring/summer period (25 May 2012, 6 August 2012) when surface albedo was dominated by vegetation. The remaining day (10 January 2013) was in winter with a fresh snow albedo.

Surface albedos for the spring/summer measurement period were determined by scaling a measured, spectral albedo of a vegetated surface (Michalsky et al., 2003) (Fig. 3). This scaling matched the 16 day average surface albedo from MODIS for Boulder, Colorado, at the discrete spectral bands 470 nm, 555 nm, 645 nm, 858 nm, 1240 nm, 1640 nm, and 2130 nm. We linearly interpolated between these bands and linearly extrapolated to shorter wavelengths to span the observed spectral range of SSFR. We applied this scaling to obtain the 16 day average surface albedo centered on 24 May 2012, on 4, 12, 20 August 2012, and on 13 September 2012 which spans our spring/summer measurement period (Fig. 3). We determined winter surface albedo (not shown) in a similar manner using a reference fresh snow surface albedo (Wiscombe and Warren, 1980) and scaling it to the retrieved albedo from MODIS for 10 January 2013 in the manner described above. The cloud base height was determined with the Skywatch ceilometer measurements and cloud top height from GOES and MODIS.

4.3 Modeled look-up-tables (LUT)

A set of modeled radiance spectra for varying τ, r_e, and ϕ (presented above) is used to build a grid of spectral parameters (described in Sect. 4.5) commonly referred to as look-up-tables (LUT). The modeled radiance spectra were interpolated to a finer grid in τ (resolution of 1) and r_e (resolution of 1 μm). For each of these interpolated

radiance spectra, we calculate the 15 parameters. This LUT of parameters is calculated for multiple solar zenith angles with resolution 0.05 in cosine of the solar zenith angle, ranging from 0.6 to 0.75 for case A, 0.6–0.7 for case B, and 0.4–0.45 for case C.

4.4 Variability in normalized radiance spectra due to τ, r_e, and ϕ – physical basis

The spectral features in cloud transmittance that vary with bulk liquid and ice absorption (Fig. 4a) and asymmetry parameter spectrum (Fig. 4b) were chosen as the basis for deriving the 15 parameters. The bulk ice absorption spectrum has local maxima that are shifted to longer wavelengths than maxima in liquid water absorption, themselves shifted to longer wavelengths than the absorption maxima in water vapor (Fig. 4a). Cloud-transmitted radiation at absorption maxima (for gas, liquid, and ice) is reduced more than the radiation at the surrounding wavelengths. For absorption by cloud particle, this is also dependent on particle size. Further reduction occurs due to multiple scattering within cloud, the amount of which depends upon cloud optical thickness. Asymmetry parameter is a measure of the ratio of forward- to back-scattering. The asymmetry parameter for ice crystals is generally lower than for liquid droplets of equivalent effective radius (see Fig. 4b), meaning that radiance transmitted through an ice cloud is consistently lower than radiance transmitted through a liquid cloud with the same optical thickness.

By modulating scattering and absorption properties of cloud particles, combinations of τ, r_e, and ϕ result in unique cloud-transmitted radiance spectra (Fig. 4). In general, the largest variability throughout the entire wavelength range, outside of the gas absorption bands, is controlled by changes in τ. By normalizing each radiance spectra by its maximum, the broad range in magnitude due to τ (considered to be the first-order dependence on τ) evident in Fig. 5a is virtually eliminated in Fig. 5b. The broad range in magnitude in the near-infrared (NIR, wavelengths longer than 700 nm) due to τ is also eliminated when normalizing each radiance spectrum by its value at 1000 nm. An added benefit of using normalized radiance is the reduction in uncertainty from 8 % for

S. E. LeBlanc et al.

Title Page

Abstract | Introduction

Conclusions | References

Tables | Figures

◀ | ▶

◀ | ▶

Back | Close

Full Screen / Esc

Printer-friendly Version

Interactive Discussion

radiance to 4.6 % for its maximum-normalized counterpart. In addition, the change in magnitude of radiance spectra in the NIR due to variation in solar zenith angles up to 80° is nearly eliminated by normalizing the radiance spectra (not shown).

After normalization, the first-order dependence of the radiance spectra on τ is re-moved, but variability in spectral radiance linked to spectral features that differ for r_e, ϕ, and τ remains. By normalizing the radiance spectra, spectral features and shapes are amplified while the large scale variation in magnitude of the radiance spectra is eliminated (see Fig. 5). In some cases, the remaining spectral features, particularly in the NIR, become more distinct for normalized radiance spectra than non-normalized radiance spectra. One such case occurs for an ice cloud of $\tau = 10$ (dashed red line), which coincides in the NIR with a liquid cloud of $\tau = 50$ (solid blue line) (Fig. 5a). How-ever, once normalized, these two clouds can be distinguished by their NIR spectral features (Fig. 5b): location of the local maximum is at 1050 nm for the liquid cloud (solid blue line) and at 1000 nm for the ice clouds (dashed red line); lower magnitude in normalized radiance near 1200 nm for the liquid than ice cloud; and steeper spectral slope near 1600 nm for the liquid than ice cloud.

Not all τ dependence is eliminated by normalization, especially at wavelengths near the liquid and ice absorption maxima in the NIR (see Fig. 4a). The effects of absorp-tion in the NIR are amplified with increases in τ, illustrated by the large variability of normalized radiance in the NIR in Fig. 6. For clouds with $\tau > 4$, the radiance in the NIR decreases with increasing τ and asymptotes to zero. The amount by which the NIR radiance is decreased is due to the absorption by cloud particles.

Not only does an increase in τ reduce the NIR transmitted signal (hereafter, trans-mittance), differences in spectrally dependent absorption also result in features that become more distinct with increases in τ (Fig. 6). Transmittance is defined here as the transmitted radiance normalized by the maximum signal rather than top-of-cloud spec-tral radiance; note that for our purposes, the features characterizing the transmitted spectra would not change for either definition of transmittance, but may differ in magni-tude. As examples of spectral features linked to differences in liquid and ice absorption,

we examine three wavelength ranges: (1) 950–1100 nm, (2) 1150–1350 nm, and (3) 1450–1650 nm. The location of the peak radiance in region (1) shifts from 1000 nm to 1060 nm as τ increases for liquid clouds (Fig. 6a). In the same wavelength range, radiance transmitted through an ice cloud has a local radiance minimum that deepens with increases in τ. Another spectral feature is observed in normalized radiance transmitted through ice clouds in the wavelength range (2) where radiance at wavelengths longer than 1200 nm is preferentially absorbed. As τ increases, the normalized radiance in region (2) changes from a convex shape with a local maximum at 1230 nm, to a concave shape with a local minimum. The spectral feature in range (3) is a curved shape with a maximum near 1500 nm that flattens with increases of τ for both ice and liquid clouds.

Since these spectral features are linked to absorption, whenever the transmittance is entirely attenuated, these features disappear. This attenuation occurs at lower τ for ice clouds than liquid clouds in the wavelength range 1500–1600 nm (see Fig. 6). This is caused by higher ice absorption than liquid in that wavelength range (see Fig. 4a). Transmittance through ice clouds at 1250 nm is also entirely attenuated at lower τ than at 1180 nm, because of higher absorption at 1250 nm than 1180 nm.

For clouds with $\tau < 4$, where radiance in the midvisible is still increasing with τ, the transmittance spectra show an influence from molecular scattering. The spectra in Fig. 6a for $\tau = 0.2$ matches more closely the clear sky spectra, which is inversely proportional to the 4th power of the wavelength, than the normalized radiance spectra for $\tau = 100$, which is roughly proportional to the inverse of the wavelength. As τ is reduced, the magnitude of signal at wavelengths between 550 nm and 700 nm decreases and its slope becomes more negative, until they match the spectrum of clear sky. The clear sky spectrum (green spectrum in Fig. 6a) is entirely dependent on scattering by molecules (Rayleigh scattering) and the solar zenith angle. The slope of the spectrum in the visible is proportional to τ until scattering by cloud particles dominates scattering by molecules. This transition occurs at lower τ for ice clouds (near 1) than liquid clouds (near 2), obscured by radiance transmitted through optically thicker clouds in

Fig. 6. After this transition, the slope of normalized radiance in the visible varies less and depends on τ, r_e, and ϕ, rather than on molecular scattering.

The normalized spectra are modified by ϕ and r_e, especially in the 3 wavelength ranges which show variations with τ. Changes of transmittance due to ϕ and r_e, when τ is kept constant, can be observed in Fig. 7. Outside of these 3 wavelength ranges and gas absorption bands, transmittance through both liquid and ice clouds overlaps for all cloud particle sizes, except for particles smaller than 5 µm. In the 3 wavelength ranges, ice and liquid clouds can be distinguished by the shape and magnitude of the transmittance. Transmittance for ice clouds has the largest dynamic range with r_e in the wavelength regions (1) and (2), while for liquid clouds it varies the most with r_e in the wavelength region (3) (see Fig. 7). In the wavelength range (1), the local minimum observed for ice clouds deepens as cloud particle sizes increase, whereas liquid water cloud transmittance does not produce a local minimum. For the spectral range (2), transmittance through a liquid cloud with distinct r_e (denoted by the thin lines with different shadings of blue in Fig. 7) varies only by the mean magnitude. In the same range, the peak signal at 1230 nm for ice clouds (denoted by different shadings of orange in Fig. 7) vanishes for largest r_e, resulting in a concave shape. Transmittance in (3) asymptotes to 0 for ice clouds, but not for liquid water clouds. The magnitude and spectral slope of liquid water cloud transmittance in (3) are reduced as r_e increases.

4.5 Definition of spectral parameters

To quantify the spectral features discussed in Sect. 4.4, we introduce 15 parameters, designated by η_1 through η_{15}, with distinct spectral transmittance characteristics that will be used to infer cloud properties. The features represent the largest patterns of variations (outside of those due to water vapor) that were observed in a set of over 800 000 cloud transmittance spectra spanning 15 days. In order to minimize the influence of water vapor on the cloud retrieval, wavelength ranges were restricted to those where water vapor absorption changed the signal by less than 5 % for precipitable

water ranging from 0 mm to 40 mm. This is a far larger range of precipitable water observed over Boulder, where the mean is about 11 mm.

The largest variability in spectral features is found in the 3 wavelength regions identified in Figs. 6 and 7, and has been quantified by 13 of the 15 parameters, where both absorption and scattering processes modulate transmittance. The transmittances in a subset of wavelengths used to calculate the first 3 parameters are highlighted in Fig. 8. The first spectral feature is the peak radiance in the wavelength range (1). It is quantified by the curvature of the radiance spectrum, normalized by the radiance at 1000 nm, and denoted by parameter 1, or η_1. The curvature is calculated from the area bounded by the transmittance and a linear interpolation between 1000 nm and 1100 nm, and is the sum of the difference between the transmittance and the linear interpolation at every wavelength. It is represented by the shaded area in Fig. 8. As τ increases, the shaded area for liquid clouds increases (for ice clouds, it decreases), which consequently increases (decreases) η_1. The change in spectral transmittance through ice clouds in (2), which is transformed from convex to concave curvature around 1230 nm as τ increases, is quantified by the 2nd parameter, η_2. This parameter is the spectral derivative of transmittance at 1200 nm, at the edge of the convex/concave shape with a maximum/minimum at 1230 nm. η_2 is identified by "2" and is highlighted to illustrate the trend with varying τ for ice clouds in Fig. 8. The spectral feature in (3), the curvature, is diminished as τ increases. This spectral feature is quantified with parameter η_3. η_3 is defined by the spectral derivative of transmittance at 1500 nm, which decreases with increasing τ for both ice and liquid clouds.

10 more parameters were defined to quantify the similar spectral features in the 3 wavelength ranges. η_7, η_9, η_{12}, and η_{13} are defined within region (1) by the mean magnitude of normalized radiance (η_7); the slope of the spectral derivative (η_9); the value of the normalized radiance at one wavelength (η_{12}); and the ratio of radiances at two different wavelengths (η_{13}). In region (2), 3 additional parameters were defined by: the ratio of radiances at two different wavelengths (η_4); the mean magnitude of normalized radiance (η_5); and the slope of the spectral derivative (η_{10}). For region (3), η_8 quantifies

the curvature by the same method described for η_1. In addition, η_6 and η_{15} quantify the mean normalized radiance and the spectral slope in region (3), respectively. The equations used calculate all 15 spectral parameters, and short descriptions of the spectral parameter with expected behavior are listed in Table 1.

The characteristics in a fourth spectral region, between 530–610 nm exhibiting spectral variability in cloud transmittance are the basis for defining an additional parameter. For transmittance from clouds with $\tau < 4$, the spectral slope in this regions becomes progressively more negative and the magnitude of transmittance decreases as τ decreases, until it reduces to the clear sky spectrum (see Fig. 9a). η_{11} quantifies the spectral slope of normalized radiance between 530 nm and 610 nm, highlighted in Fig. 9a. The slopes calculated from these and other normalized spectra increase with τ until a maximum is reached (see Fig. 9b) at a value of $\tau \sim 3$ for ice clouds and τ up to 7 for liquid clouds. The spectral behavior in this fourth spectral region is modulated by changes in scattered radiation.

4.6 Dependence on thermodynamic phase, optical thickness, and effective radius

The dependencies of the 15 parameters (Sect. 4.5; Table 1) on τ for ice clouds (dashed) and liquid clouds (solid) and for 3 different particle sizes are shown in Fig. 10. The accuracy for each of the parameters is estimated by propagating the measurement accuracy through the formula in Table 1. Modeled spectra are evaluated with the variation of SSFR's 3 radiometric calibrations and their related precision (Sect. 2.1). The standard deviation of the set of spectral parameters calculated from these modeled spectra is represented by the shaded area for each parameter in Fig. 10.

Parameter sensitivity to τ, r_e, and ϕ is larger than the measurement uncertainty (see Fig. 10), for several parameters, clearly establishing their suitability for distinguishing cloud properties. For clouds with $\tau < 10$, the most appropriate parameters are: η_3, η_8, and η_{10} ($\frac{\partial}{\partial \lambda_{1.5}}$, $C_{1.6}$, and $\frac{\partial^2}{\partial \lambda_{1.2}^2}$). For clouds with $\tau > 10$, the spectral parameters η_6 and

η_{15} ($\langle R \rangle_{1.6}$ and $sl_{1.6}$) have largest sensitivity to τ and r_e. The most suitable parameters for ice clouds are: η_1, η_2, and η_9 ($C_{1.0}$, $\frac{\partial}{\partial \lambda_{1.2}}$, and $\frac{\partial^2}{\partial \lambda_{1.0}^2}$). The largest sensitivity to τ, regardless of r_e and ϕ is found in η_{11} ($sl_{0.55}$).

4.6.1 Thermodynamic phase

Thermodynamic phase is the largest contributor to the variability in η_1, η_2, η_4, η_9, η_{10}, and η_{13} ($C_{1.0}$, $\frac{\partial}{\partial \lambda_{1.2}}$, $r_{1.2}$, $\frac{\partial^2}{\partial \lambda_{1.0}^2}$, $\frac{\partial^2}{\partial \lambda_{1.2}^2}$, and $r_{1.0}$, respectively). This is shown by the separability between the values of these parameters evaluated for a liquid cloud compared to an ice cloud (see Fig. 10). These parameters exploit spectral features that depend on cloud phase in the wavelength ranges (1) and (2); see Fig. 7. The differences between spectral features for each cloud thermodynamic phase are due to variations in absorption, which are more pronounced for the largest optical thicknesses, and changes in scattering properties to which clouds with the smallest optical thickness are the most sensitive.

The parameters η_1, η_9, and η_{13} ($C_{1.0}$, $\frac{\partial^2}{\partial \lambda_{1.0}^2}$, and $r_{1.0}$) quantify spectral features in the wavelength range (1). Along with η_1, η_9 also calculates the curvature but by the slope of spectral derivative, where negative values of η_1 and positive values of η_9 are attained only by ice clouds. Values of η_{13}, lower than 1 are obtained by normalized radiance spectra transmitted through liquid clouds.

In the wavelength range (2), the transmittance for either ice and liquid water cloud result in large differences in the parameters η_2, η_4, and η_{10} ($\frac{\partial}{\partial \lambda_{1.2}}$, $r_{1.2}$, and $\frac{\partial^2}{\partial \lambda_{1.2}^2}$).

Values of η_2 for liquid water clouds are never lower than $-0.35\,\mu m^{-1}$ and vary little, whereas only ice clouds values as low as $-21.2\,\mu m^{-1}$ (Fig. 8). The large change in η_2 for ice clouds compared to liquid water clouds is due to a local maximum of absorption slightly longward of 1200 nm for ice but not for liquid water. These values hold for the ranges in surface albedo, cloud base height, atmospheric state, and solar zenith angle

represented during the cases 25 May 2012 and 6 August 2012. Another measure of the spectral feature in (2) is the ratio of radiance at 1200 nm and 1237 nm (η_4), which increases to as high as 18.8 with increases in ice cloud τ, but varies much less with changes in liquid water cloud properties. The signal to noise ratio of η_4 is reduced be-

5   low 1 for large ice cloud τ where the radiance at 1237 nm is entirely attenuated. The curvature of normalized radiance in (2), quantified by η_2, is also quantified by the slope of the spectral derivative, η_{10}, which increases (decreases) with optical thickness for ice (liquid) clouds. When transmittance is nearly entirely attenuated ($\tau > 40$), the concave and convex shapes become less pronounced; therefore, η_{10} decreases for ice

10 clouds, and increases for liquid clouds.

4.6.2   Optical thickness

Parameters η_3, η_5, η_6, η_7, η_8, η_{11}, η_{12}, η_{14}, and η_{15} ($\frac{\partial}{\partial\lambda_{1.5}}$, $\langle R \rangle_{1.25}$, $\langle R \rangle_{1.6}$, $\langle R \rangle_{1.0}$, $C_{1.6}$, sl$_{0.55}$, $R_{1.04}$, $r_{0.6}$, and sl$_{1.6}$) are most sensitive to changes in τ. At $\tau < 5$, scattered radiation is the primary contributor to change in η_5, η_6, η_7, η_{11}, η_{12}, and η_{14}, and it varies

15 with τ (see Fig. 10). Of these parameters, η_5, η_6, η_7, and η_{12} quantify the magnitude of transmittance in all 3 wavelength ranges. Of the remaining parameters, η_{14}, quantifies the same spectral feature presented in Fig. 9 and quantified by η_{11}. Unlike η_{11}, the influence of the underlying surface albedo on η_{14} increases with increasing τ at $\tau > 5$, as expected by the physical process described by Chiu et al. (2006).

20   For $\tau > 5$, the spectral features that are quantified by η_3, η_5, η_6, η_7, η_8, and η_{12} ($\frac{\partial}{\partial\lambda_{1.5}}$, $\langle R \rangle_{1.25}$, $\langle R \rangle_{1.6}$, $\langle R \rangle_{1.0}$, $C_{1.6}$, and $R_{1.04}$) are increasingly dominated by absorption. This causes a reduction in the magnitude of normalized radiance, evaluated by η_5, η_6, η_7, and η_{12}. η_3, η_8, and η_{15} ($\frac{\partial}{\partial\lambda_{1.5}}$, $C_{1.6}$, and sl$_{1.6}$) quantifies the change in (3) due to ice and liquid water absorption, which is enhanced with increasing τ due to higher order

25 scattering. When the shape of transmittance flattens, η_3 and η_8 decrease, while η_{15} increases.

Cloud property retrieval using transmitted spectra

S. E. LeBlanc et al.

Title Page

Abstract | Introduction

Conclusions | References

Tables | Figures

|◄ | ►|

◄ | ►

Back | Close

Full Screen / Esc

Printer-friendly Version

Interactive Discussion

4.6.3 Effective radius

Effective radius contributes to variability in all 15 parameters. In particular, η_1 to η_{10}, η_{12}, η_{13}, and η_{15} quantify the spectral features that are linked to absorption modified by r_e, while η_3, η_5 to η_8, η_{11}, and η_{15} quantify the changes in the spectral features due to the changes in scattering properties of different r_e. η_1, η_2, η_3, η_4, η_9, η_{10}, η_{13}, and η_{15} ($C_{1.0}$, $\frac{\partial}{\partial \lambda_{1.2}}$, $\frac{\partial}{\partial \lambda_{1.5}}$, $r_{1.2}$, $\frac{\partial^2}{\partial \lambda_{1.0}^2}$, $\frac{\partial^2}{\partial \lambda_{1.2}^2}$, $r_{1.0}$, and $\mathrm{sl}_{1.6}$) quantify spectral features that are unique to absorption, which increases with particle size at any one τ. In the wavelength range (1), the separation between liquid water and ice values of η_1, η_9, and η_{13} increases with r_e. η_2, η_4, and η_{10} parameterize the transmittance feature in (2) linked to r_e-dependent ice particle absorption, but not liquid water absorption. For η_{15}, absorption decreases from 1565 nm towards longer wavelengths (McBride et al., 2011) resulting in a dependence on r_e, also quantified by η_3 in the same wavelength region. Cloud particle size affects η_3, η_5, η_6, η_7, η_8, and η_{12} ($\frac{\partial}{\partial \lambda_{1.5}}$, $\langle R \rangle_{1.25}$, $\langle R \rangle_{1.6}$, $\langle R \rangle_{1.0}$, $C_{1.6}$, and $R_{1.04}$) by modulating the spectral features through scattering and absorption. These spectral parameters are consistently higher at any one τ and ϕ for the smallest r_e, regardless if it is scattering or absorption that dominates.

5 Retrieval methodology

For any transmittance spectrum, a single spectral parameter is insufficient to derive τ, r_e, and ϕ. Multiple spectral parameters can be used to first identify thermodynamic phase (ϕ), followed by another procedure employing additional parameters, to derive τ and r_e. Eq. (1) is the statistic, $\chi^2(\tau, r_e, \phi)$, used to retrieve τ and r_e from a weighted least-squares-fit between modeled and observed values of all 15 parameters ($i = 1, 2, 3, \ldots, 15$). The retrieval is defined at the closest match (minimum in χ^2) between measurement-derived parameters, η_i, and the parameters derived from forward-model LUT $\boldsymbol{\eta}_i^*(\tau, r_e, \phi)$ at cosine of the solar zenith angle closest to that of the

observation.

$$\chi^2(\tau, r_{\mathrm{e}}, \phi) = \sum_{i=1}^{15} \frac{1}{w_i} \left(\boldsymbol{\eta}_i - \boldsymbol{\eta}_i^*(\tau, r_{\mathrm{e}}, \phi) \right)^2 \tag{1}$$

In order to properly weight the contributions from each parameter, a factor, w_i, is de-rived from the full range of the parameters, P_i. Not all parameters can be determined with equal certainty; therefore, the measurement uncertainty, $\Delta\eta_i$, of each parameter is also included in the weighting factor in a manner similar to Wan and Li (1997), where the most uncertain parameter has lowest influence on the solution.

$$w_i = \Delta\boldsymbol{\eta}_i P_i \tag{2}$$
$$P_i = \max(\boldsymbol{\eta}_i^*(\tau, r_{\mathrm{e}}, \phi)) - \min(\boldsymbol{\eta}_i^*(\tau, r_{\mathrm{e}}, \phi)) \tag{3}$$

Therefore, the maximum contribution of each parameter to $\chi^2(\tau, r_{\mathrm{e}}, \phi)$ is 1; the theoret-ical maximum value of $\chi^2(\tau, r_{\mathrm{e}}, \phi)$ is 15. The full range of each parameter is obtained by the maximum and minimum of the LUTs.

The retrieval process consists of two steps. In the first step, thermodynamic phase, ϕ, can be discriminated by using a single parameter or with the combination of all 15 parameters. η_1, η_2, η_4, η_9, η_{10}, and η_{13} ($C_{1.0}$, $\frac{\partial}{\partial\lambda_{1.2}}$, $r_{1.2}$, $\frac{\partial^2}{\partial\lambda_{1.0}^2}$, $\frac{\partial^2}{\partial\lambda_{1.2}^2}$, and $r_{1.0}$) return unique values for either ice or liquid clouds for clouds with optical thickness larger than 10. Positive values for η_9 and η_{10}, negative values for η_1, and values below $-0.35\,\mu\mathrm{m}^{-1}$ for η_2 are unique to ice clouds, for the environmental conditions (ancillary inputs) de-scribed in Sect. 4.2. Outside this range, both ice and liquid water clouds produce the same parameters, and thus ϕ cannot be discriminated with a single parameter. For all clouds with τ lower than 10 (as r_{e} increases, this cutoff in τ decreases), a combination of all 15 parameters is used to determine ϕ by the best-fit LUT solution identified at the minimum χ^2 defined in Eq. (1). Although multiple parameters are required to discrimi-nate ϕ, this does not mean that ϕ is any less certain than when using a single spectral parameter.

Once ϕ is determined, a second step consists of a ϕ-segregated retrieval of τ and r_e. To apply the ϕ-segregated retrieval, we use the LUT of the appropriate ϕ (either $\boldsymbol{\eta}_i^*(\tau, r_e, \phi = \text{ice})$ or $\boldsymbol{\eta}_i^*(\tau, r_e, \phi = \text{liquid})$). The LUTs for ice or liquid clouds are defined with different ranges in r_e, which represent naturally occurring ice or liquid cloud particle size (see Sect. 4.3). The retrieved τ and r_e represents the location in the LUT which defines minimum χ^2, calculated from Eq. (1).

When determining χ^2, some of the 15 parameters calculated from the measured spectrum do not fall within the range of the LUT. The parameters that do not fall within the LUT are deemed non-physical and are therefore omitted from the calculation of χ^2. Values outside the LUT occur when the signal to noise ratio of the parameter is lower than one, or it is at the limit of ranges within the LUT. An example of small signal to noise ratio occurs for η_4 when evaluated for ice clouds with $\tau > 65$ and $r_e > 30\,\mu\text{m}$; see the large shaded area in Fig. 10. Since each parameter results from different physical processes, the signal to noise ratio may be lower than one for certain parameters but not for others (for example, η_4 compared to η_9 for ice clouds with $\tau > 65$). Therefore, the solution may still be valid, even without the contributions from uncertain parameters.

A successful retrieval occurs when the parameters calculated from a measurement spectrum matches those modeled for at least one combination of τ, r_e, and ϕ. This match is defined where the minimum χ^2 is lower than predefined value, 0.69. This value represents 4.6 % of the total theoretical maximum χ^2, which is the same percentage as the measurement uncertainty in normalized radiance spectra (see Sect. 2.1).

5.1 Retrieval uncertainty

To obtain the retrieval uncertainty of τ and r_e, we propagate measurement uncertainty through the retrieval equation. The uncertainty in the parameters, $\Delta\eta_i$, and the slope of χ^2 as a function of the parameters quantify the expected variation in χ^2 resulting from

measurement uncertainty, described by $\Delta\chi^2$ (adapted from Taylor, 1997).

$$\Delta\chi^2(\tau, r_e, \phi) = \sqrt{\sum_{i=1}^{15}\left(\frac{\partial\chi^2(\tau, r_e, \phi)}{\partial\boldsymbol{\eta}_i}\Delta\boldsymbol{\eta}_i\right)^2} \tag{4}$$

This expected variation in χ^2 due to measurement uncertainty ($\pm\Delta\chi^2$) results in a range of τ and r_e where $\chi^2 \pm \Delta\chi^2$ is minimized. The minimum $\chi^2 - \Delta\chi^2$ (or $\chi^2 + \Delta\chi^2$) occurs at the combination of $\tau|_{\chi^2-\Delta\chi^2}$ (or $\tau|_{\chi^2+\Delta\chi^2}$) and $r_e|_{\chi^2-\Delta\chi^2}$ (or $r_e|_{\chi^2+\Delta\chi^2}$). The difference between τ and r_e evaluated at the extremes of the range of variability of χ^2, represent their respective uncertainty, $\Delta\tau$ and Δr_e.

$$\Delta\tau = \frac{1}{2}\left|\tau|_{\chi^2-\Delta\chi^2} - \tau|_{\chi^2+\Delta\chi^2}\right| \tag{5}$$

$$\Delta r_e = \frac{1}{2}\left|r_e|_{\chi^2-\Delta\chi^2} - r_e|_{\chi^2+\Delta\chi^2}\right| \tag{6}$$

5.2 Comparisons to other methods

The retrieval described herein is compared to two other methods: the method developed by McBride et al. (2011), hereafter named the slope method, and the standard 2-wavelength method often used in reflectance (Nakajima and King, 1990) but applied to transmittance as described by Kikuchi et al. (2006), hereafter named the 2-wavelength method.

5.2.1 Slope method

The slope method uses transmittance at 515 nm and the slope of transmittance at 1565–1634 nm normalized by the transmittance value at 1565 nm to retrieve τ and r_e. A least squares fit matches measured transmittance and slope values to a LUT containing modeled transmittances and slopes for a set of τ and r_e. The retrieval is

successful if the uncertainty in r_e is smaller than 2 µm. The LUTs used for this retrieval method are based on the same radiative transfer calculations introduced in Sect. 4.1. For cases A and B, the slope method is applied using a liquid cloud LUT, while for case C, an ice cloud LUT is used. Case C represents the first time the method described by McBride et al. (2011), is applied to an ice cloud. For this case, all retrieved values are presented, even if the uncertainty in r_e is larger than 2 µm.

5.2.2   2-wavelength method

The 2-wavelength method retrieves τ and r_e using transmittance at wavelengths in the mid-visible (515 nm) and in the near-infrared (1630 nm) with a LUT, similarly to the current work's method and the slope method. Kikuchi et al. (2006) employed transmittance evaluated at 1020 nm and 1600 nm. For this work, we follow the description of the "standard" method presented by McBride et al. (2011), which employs transmittance at 515 nm and 1630 nm to retrieve τ and r_e. Although the 2-wavelength method produces large uncertainties in r_e when applied to clouds with $\tau < 25$, we still apply it here, and report the associated uncertainties. The uncertainties in τ and r_e are calculated by the same method described by McBride et al. (2011), but applied to the measurement uncertainty of the SSFR (8 %) used in this work. Similarly to the slope method, the 2-wavelength retrieval employs a liquid water cloud LUT for cases A and B and an ice cloud LUT for case C.

5.2.3   Comparison of time series

Figure 11 shows the time series of τ, r_e, and ϕ retrieved using the 15-parameter method (this work), the slope retrieval, and the 2-wavelength retrieval based on transmitted radiance for the (A) liquid, (B) mixed-phase, and (C) ice cloud cases.

The ancillary data (discussed in Sect. 4.2) and the 15-parameter method classified each case consistently with respect to the thermodynamic phase. The τ retrieved with all 3 methods follows similar trends, albeit with different magnitudes. One exception

is the start of case B, where the 15-parameter method retrieved ice clouds with much lower τ than the other two methods. The retrieved r_e based on all 3 methods also follow the similar trends; again, the onset of case B is anomalous, as is the 2-wavelength method in case C. In addition, the uncertainty in the 15-parameter method retrievals is lower than that for the other two methods, especially for case C, with an average r_e uncertainty of $\pm 1.2\,\mu m$ smaller by a factor of at least 2.5 for the slope and 2-wavelength method respectively.

For case A, the 15-parameter method retrieved τ matches more closely to the 2-wavelength method (mean difference of 2.5) than the slope method (mean difference of 5.6), while the retrieved r_e matches more closely the slope method (mean difference of 2.6 μm) then the 2-wavelength method (mean difference of 4.4 μm). The largest differences occur between τ retrieved with the 15-parameter method and τ retrieved with the slope method, whenever the 15-parameter τ is larger than 30. The range of τ retrieved with all three methods is never larger than 8 for the times between 15:00–15:40 UTC. This period coincides with times where the uncertainty in τ for the 15-parameter method is lowest, with a mean of ± 1.2 and the average retrieved τ is highest at 32. This mean uncertainty increases to ± 2.6 for later times, where the average τ decreases to 28. The slope and 2-wavelength method retrieved an uncertainty of τ consistent throughout the measurement period, with averages of ± 1.3 and ± 1.5 respectively. Additional comparisons for this case are presented below.

Similarly to the comparison of τ for case A, the effective radii retrieved by all 3 methods matches more closely (within 5 μm) during the period from 15:00–15:40 UTC than the later period (within 10 μm). The uncertainty of r_e for all 3 methods is also lower in the earlier period (a mean of $\pm 1\,\mu m$ for all 3 methods) than the later period (a mean of $\pm 1.9\,\mu m$). Higher-than-average r_e uncertainty coincides with retrieved-τ lower than 20 for all 3 methods. Such behavior for low τ has been observed previously for the slope and 2-wavelength method (Coddington et al., 2013; McBride et al., 2011). The r_e retrieved with the current work is within the uncertainty range of r_e retrieved with the 2-wavelength method for 27 % and the slope method for 69 % of the time series.

Title Page

Abstract | Introduction

Conclusions | References

Tables | Figures

Back | Close

Full Screen / Esc

Printer-friendly Version

Interactive Discussion

Case B presents examples of retrieval behavior under conditions of liquid and ice cloud particle absorption. Although we have not addressed the applicability of the 15 spectral parameters to mixed phase clouds in this work, we investigate the results of the thermodynamic phase discrimination, and the residual of least squares fit of the retrieval to measured transmittance under conditions of concurrent ice and liquid absorption. The thermodynamic phase retrieval coincides with the thermodynamic phase retrieved by GOES, which was ice prior to, and liquid during, the measurement period. The largest χ^2 occurs between 22:20 UTC and 22:40 UTC, when the thermodynamic phase transitions from an ice cloud to a liquid cloud, as determined by the 15-parameter method. In this transition zone, only 40 % of the solutions obtained by the retrieval described herein are valid. Large residuals indicate that more information is required to reproduce the parameters calculated from the measurements of transmittance spectra. Beyond this transition period, the match between τ retrieved from all 3 methods is exceptional, especially since none of the retrievals explicitly takes into account mixed-phase clouds. The overall trend is reproduced with all 3 retrieval methods and they differ by an average of 5.8 in retrieved τ and 4.7 μm in retrieved r_e, for the period later than 22:40 UTC. At these times, uncertainties in r_e are greater than ±2 μm for 13 % of the time series for the current method, 26 % for the slope method and 44 % for the 2-wavelength method.

For case C, the match in τ retrieved with all 3 methods differs by less 3 throughout the entire time series even though the retrieved r_e differs by as much as 37 μm. The r_e uncertainty is larger than ±2 μm at all times for the slope method, 62 % of the time series for the 2-wavelength method, and 29 % of the time series when retrieved with the 15-parameter method. These large uncertainties obtained from the slope and 2-wavelength method are likely due to a lower signal to noise ratio of ice cloud transmittance compared to a liquid water cloud transmittance near 1600 nm. This low signal can be observed in the ice cloud transmittance spectrum for a $\tau = 10$ with $r_e = 20$ μm (Fig. 5a). The smaller r_e uncertainties obtained by the 15-parameter method compared to the slope and 2-wavelength retrieval is also expected. Specific parameters were

designed to take advantage of features that have high signal to noise ratio for ice and liquid clouds (e.g., η_1 ($C_{1.0}$), η_2 ($\frac{\partial}{\partial \lambda_{1.2}}$), η_9 ($\frac{\partial^2}{\partial \lambda_{1.0}^2}$), η_{10} ($\frac{\partial^2}{\partial \lambda_{1.2}^2}$), and η_{13} ($r_{1.0}$)).

During the ice cloud case C, MODIS observed the same cloud at 18:17 UTC. Keep in mind that τ and r_e retrieved by MODIS were from sampling volume close to cloud top,
unlike the transmittance based 15-parameter method. Note also the spatial resolution of MODIS, $1\,km^2$, vs. that of the zenith-pointing SSFR, estimated to be $0.45\,km^2$ for a cloud base at 7.5 km. At 18:17 UTC, the 15-parameter method retrieved $\tau = 8 \pm 0.5$ and $r_e = 30 \pm 2\,\mu m$, while MODIS retrieved $\tau = 12.7 \pm 15.3$ and $r_e = 17.1 \pm 5.4\,\mu m$ with "very good confidence" for both τ and r_e retrievals (Platnick et al., 2003). The 15-
parameter τ retrieval falls within the uncertainty range of MODIS. The difference in retrieved r_e is likely due to the difference between particle sizes at cloud top and particle sizes throughout the cloud. Both the slope and 2-wavelength methods resulted in a retrieval with an r_e-uncertainty larger than $2\,\mu m$ at this time.

5.2.4 Comparison of retrieved τ and r_e for the liquid cloud case

All 3 retrievals for case A exhibit a high degree of correlation. The linear correlation coefficient (R^2) between the 15-parameter method and the other methods is 0.95 for τ, but lower for r_e (see Fig. 12). The τ retrieved with the slope and 2-wavelength methods are consistently higher than the 15-parameter τ. The difference between the 15-parameter method and the two other methods increases linearly with increasing τ by a ratio of
1.28 and 1.10 for the slope and 2-wavelength methods, respectively (Fig. 12a). For r_e (Fig. 12b), the 2-wavelength method retrieves lower r_e than the 15-parameter method by a ratio of 0.81; the slope method does not have such a low bias with respect to r_e retrieved by the current method. A greater correlation between τ than r_e, retrieved with the different methods, was also observed by McBride et al. (2011) for the 2-wavelength
and slope retrievals.

For this liquid cloud case, factors contributing to differences in retrieved r_e values include varying effects of vertical profiles in r_e evaluated at different wavelengths

(Platnick, 2000), horizontal cloud inhomogeneities (e.g., Iwabuchi and Hayasaka, 2002; Marshak et al., 2006), and undetected presence of ice crystals (Sun and Shine, 1994). Although transmitted radiation interacts with cloud particles throughout the vertical extent of a cloud, this interaction is not the same for radiance at all wavelengths.

5   Platnick (2000) shows that cloud particles in the lowest part of the cloud have a greater influence on transmittance for wavelength at 3700 nm than at 2200 nm, and even less influence on transmittance at 1600 nm. Those cloud particles are responsible for changes in transmitted irradiance of up to 6 % at those wavelengths. This would suggest that cloud retrievals based on transmittance at shorter wavelengths would be less

10 dependent on absorption and scattering by cloud particles in the lowest part of the cloud than transmittance at longer wavelengths. Although the influence of the cloud particles near cloud base on the different parameters has not been determined, one would expect that the parameters based on mean normalized radiance at wavelengths shorter than 1600 nm would be less influenced by particles at cloud base than the 2-

15 wavelength method. For liquid clouds, the smallest cloud particles are often located near base (e.g., Zhang et al., 2011); therefore, the 15-parameter method would retrieve larger r_e than the 2-wavelength method. For case A, the 15-parameter method retrieved larger r_e than the 2-wavelength method for 81 % of the times, which could in part be due to the spectral dependence of vertical distribution of cloud particle size on

20 transmitted radiance. In addition, Kikuchi et al. (2006), showed that clouds with vertically varying particle size can change the retrieved τ by up to 2 %.

Cloud inhomogeneities may also affect the 3 retrieval methods in different ways. For case A, the time period selected for analysis reduced, but did not entirely eliminate, horizontal cloud inhomogeneities. For example, τ varied between 25 and 43 within

25 15 min around 15:40 UTC (Fig. 11). Cloud inhomogeneity has caused overestimations of cloud particle size for reflectance based retrieval due to shadowing (Marshak et al., 2006). Shadowing may also cause an overestimate of cloud particle size for transmitted radiance based retrievals. Lastly, The presence of ice crystals may have been a cause of differences between the slope and 2-wavelength methods in the work described by

McBride et al. (2011). However, it is unlikely the cause of differences in this case. Ice crystal spectral absorption and scattering features are quantified with η_1, η_2, η_9, η_{10}, and η_{13}. If such features were observed, the cloud would be identified as an ice cloud.

5.2.5 Modeled and measured radiance spectra comparison

More insight into the differences between the three retrievals is gained when selecting a single sample measurement for further analysis. We compare a representative measurement spectrum to modeled spectra derived from the retrieved τ and r_e values from all three methods in Fig. 13. For all 3 cases, the root-mean-square (rms; see Table 2) difference throughout the entire wavelength range of the measured radiance spectra and the modeled radiance spectra based on the 15-parameter method are less than the other two methods by up to a factor of 3.8 smaller. However, radiances at the shortest wavelengths (< 1000 nm) modeled using the slope method matched the measured spectra more closely than the 15-parameter method for the liquid cloud case (rms of 2.4 % vs. 3.4 %) but not for the ice cloud case (rms of 7.7 % vs. 4.9 %).

For case A (Fig. 13), the fit of all modeled radiance spectra to the measured spectra is better than 24 %, resulting in rms values smaller than 6.4 %, with the largest variation from the measured spectra occurring at the longest wavelengths (> 1000 nm). At wavelengths shorter than 1000 nm, the modeled spectra based on all three retrievals matches the measured spectrum within 12 %. At 1500 nm, the radiance difference for the modeled radiance spectra based on the slope retrieval diverges by 24 %. By contrast, the difference between measured and modeled radiance spectrum based on τ and r_e retrieved using the 15-parameter method is better than 7 % at wavelengths longer than 1000 nm outside gas absorption bands and better than 8 % at all wavelengths resulting in a rms of at least 2.8 % lower than the other two methods. The better fit is expected for the 15-parameter method since the 15 parameters quantify spectral features located at wavelengths nearly spanning the entire range.

The sample measured spectrum for case B was selected to coincide at the transition between ice and liquid cloud, where both ice and liquid cloud particles influence

the transmitted radiance spectrum. The retrieval described herein classified the cloud as liquid because the normalized radiance magnitudes indicated that the cloud was composed of liquid cloud droplets, although some ice particle absorption features are still apparent in the measured spectrum at wavelengths longer than 1000 nm. One ice absorption feature is the monotonically decreasing radiance between 1000–1100 nm, which is quantified by η_1 and η_9. Conversely, liquid cloud droplets produce a local maximum in radiance at 1050 nm. We observed this maximum in the modeled radiance spectra based on the slope, 2-wavelength, and the 15-parameter method (solid lines in Fig. 13). The ice absorption feature found in the measured radiance spectrum is reproduced in the dark green dashed line in Fig. 13, where there is no maximum at 1050 nm. Between 1500–1700 nm, the modeled ice cloud spectrum matches measurement more closely (within 16 %) than modeled liquid cloud spectrum based on the slope and 2-wavelength method (up to 28 % difference), even though the smallest rms for the entire wavelength range (7.2 %) is obtained for the liquid cloud spectrum modeled from the 15-parameter method.

For case C (Fig. 13), the modeled radiance based on the 15-parameter method reproduced the measurement at wavelengths > 1000 nm more accurately than the modeled radiance based on the other two methods, similarly to case A. The modeled radiances based on the 2-wavelength and slope method match nearly identically the measured radiance at 515 nm, but diverge by up to 55 % at wavelengths > 1000 nm. The poor fit of modeled radiance based on these 2 methods to measured radiance at longer wavelengths is likely due to the low signal to noise ratio of radiance at wavelengths near 1600 nm, where ice absorption is largest. The best fit to the measured spectrum throughout the entire wavelength range is obtained by the modeled radiance spectrum based on the 15-parameter described in this work, with an rms of 5.9 %, which is 3.8 (3.4) times smaller than the rms from the slope (2-wavelength) method. This is expected since only 4 of the 15 spectral parameters rely on radiance with low signal to noise ratio, whereas half of the information for the slope and 2-wavelength method rely on radiances at those wavelengths.

Full Screen / Esc

Printer-friendly Version

Interactive Discussion

6 Summary and conclusions

This work introduces 15 new parameters quantifying unique absorption and scattering properties of ice and liquid water cloud particles and their first application to measured cloud radiance spectra to retrieve τ, r_e, and ϕ. The 15 parameters generalize cloud retrieval techniques based on spectral radiance transmitted through clouds and were inspired by the spectral feature quantified by McBride et al. (2011). These parameters are derived from transmitted spectral radiance measurements which have been normalized by their maximum value or by the radiance value at 1000 nm. By doing this, we no longer rely on the absolute radiometric calibration, which varies up to 8 %. Rather, we rely on the much higher wavelength-to-wavelength stability of the SSFR (4.6 % or 1.1 %, depending on the normalization method). The measurements of spectral radiance were made by the SSFR based at the Skywatch observatory in Boulder, Colorado, for 3 time periods encompassing clouds of different thermodynamic phase: liquid (case A), mixed-phase (case B), and ice (case C). We retrieve τ, r_e, and ϕ by evaluating the weighted least-squares best fit between the parameters calculated from measured transmittance and precomputed tables of parameters derived from simulated cloud radiance. The new parameters are shown to distinguish cloud thermodynamic phase. This discrimination uses spectral absorption and scattering features unique to either ice or liquid water cloud particles. Thermodynamic phase discrimination for 3 cloud cases correctly reproduced the classification of the thermodynamic phase by ancillary data.

Five of the parameters, η_1, η_2, η_9, η_{10}, and η_{13}, give distinct values when either ice or liquid cloud particles are present. This sensitivity to thermodynamic phase is obtained by capitalizing on spectral differences in the absorption properties of ice and liquid cloud particles. Some of these parameters, η_9 and η_{10} for example, are defined over spectral ranges where the position of the local maximum and minimum of transmittance differs for ice or liquid clouds. In those wavelength ranges, the transmittance for ice or

liquid water clouds exhibit either a concave or convex shape, where the spectral slope increases or decreases, respectively, as wavelength increases.

The 15 parameters quantify specific spectral features found in normalized radiance. The normalization amplifies the spectral features of interest and allows for a more direct comparison of radiance spectra transmitted through different cloud, but removes the first-order dependence on τ. After normalization, the parameters still show dependence on τ, r_e, and ϕ. Of these 15 parameters, we have found that η_1, η_2, η_3, η_6, η_8, η_9, η_{10}, η_{11} and η_{15} ($C_{1.0}$, $\frac{\partial}{\partial\lambda_{1.2}}$, $\frac{\partial}{\partial\lambda_{1.5}}$, $\langle R\rangle_{1.6}$, $C_{1.6}$, $\frac{\partial^2}{\partial\lambda^2_{1.0}}$, $\frac{\partial^2}{\partial\lambda^2_{1.2}}$, $sl_{0.55}$, and $sl_{1.6}$) show the largest sensitivity to τ, r_e, and ϕ.

We compare τ and r_e from 3 different retrievals: the 15-parameter retrieval described in this work, the spectral slope method described by McBride et al. (2011), and the 2-wavelength method, which is typically used with reflectance (Nakajima and King, 1990) but applied to transmittance (Kikuchi et al., 2006). For the liquid cloud case, the τ retrieved with the 3 different methods correlated well ($R^2 = 0.95$) and matched within 10, whereas, r_e retrieved with the 3 methods did not match as well and correlated less (as low as $R^2 = 0.74$). One possible reason for the differences in retrieved r_e values can be attributed to the varying influence of cloud droplet vertical profile on radiance at different wavelength regions (Platnick, 2000).

We compared measured transmitted radiance spectra to modeled transmitted radiance spectra based on the retrieved τ, r_e, and ϕ. We find root-mean-square differences between modeled and measured radiance spectra are less when using the results from the 15-parameter retrieval (3.1 %) than the slope and 2-wavelength method, by up to a factor of 3.8 for the ice cloud case. By contrast, differences in radiances approach 6.4 % for the liquid case and 22.5 % for the ice cloud case evaluated over the same wavelength range for modeled radiances based on slope and 2-wavelength retrieval. At the shortest wavelengths (less than 1000 nm), the slope method outperform this work's method for liquid clouds, but not for ice clouds in terms of match to the measured spectra.

The use of spectral information in this work showcases the advantages of using a spectrometer system for remote sensing of clouds. Increased understanding of cloud properties can be gained using photons that have interacted with cloud particles throughout the entire cloud vertical extent. The basis of this method could also be applied to spectral reflectance measurements from satellites. Some of the spectral features investigated here may translate directly to reflectance, especially those based entirely on absorption properties of liquid and ice cloud particles. In future work, we will formally quantify uncertainties in the retrieved cloud properties from this new method and the information content of each parameter, by investigating the impact of varying ancillary inputs on the retrieval scheme. This will be done using a nonlinear methodology (Vukicevic et al., 2010) that will investigate the changes of the retrieved properties over the full range of optical thickness and effective radius that results from uncertainties in the measurement and forward model inputs.

References

Allan, R. P.: Combining satellite data and models to estimate cloud radiative effect at the surface and in the atmosphere, Meteorol. Appl., 18, 324–333, doi:10.1002/met.285, 2011. 5294

Baum, B. A., Yang, P., and Heymsfield, A. J.: The next generation of ice cloud bulk scattering/absorption models at visible through infrared wavelengths, Imaging and Applied Optics, p. HTuB2, doi:10.1364/HISE.2011.HTuB2, 2011. 5295, 5301, 5337

Chiu, C., Marshak, A., Knyazikhin, Y., Wiscombe, W. J., Barker, H. W., Barnard, J. C., Luo, Y., and Chiu, J. C.: Remote sensing of cloud properties using ground-based measurements of zenith radiance, J. Geophys. Res., 111, D16201, doi:10.1029/2005JD006843, 2006. 5310

Cloud property retrieval using transmitted spectra

S. E. LeBlanc et al.

Chiu, J. C., Huang, C.-H., Marshak, A., Slutsker, I., Giles, D. M., Holben, B. N., Knyazikhin, Y., and Wiscombe, W. J.: Cloud optical depth retrievals from the Aerosol Robotic Network (AERONET) cloud mode observations, J. Geophys. Res., 115, 1–12, doi:10.1029/2009JD013121, 2010. 5295

Coddington, O. M., Pilewskie, P., Schmidt, K., McBride, P., and Vukicevic, T.: Characterizing a new surface-based shortwave cloud retrieval technique, based on transmitted radiance for soil and vegetated surface types, Atmosphere, 4, 48–71, doi:10.3390/atmos4010048, 2013. 5296, 5316

Cumming, J. B.: Temperature dependence of light absorption by water, Nucl. Instrum. Meth. A, 713, 1–4, doi:10.1016/j.nima.2013.02.024, available at: http://arxiv.org/abs/1301.1984, 2013. 5337

Daniel, J. S.: Cloud liquid water and ice measurements from spectrally resolved near-infrared observations: a new technique, J. Geophys. Res., 107, 4599, doi:10.1029/2001JD000688, 2002. 5295

Daniel, J. S., Solomon, S., Miller, H. L., Langford, A. O., Portmann, R. W., and Eubank, C. S.: Retrieving cloud information from passive measurements of solar radiation absorbed by molecular oxygen and O_2–O_2, J. Geophys. Res., 108, 1–12, doi:10.1029/2002JD002994, 2003. 5295

Daniel, J. S., Portmann, R. W., Miller, H. L., Solomon, S., Langford, A. O., Eubank, C. S., Schofield, R., Turner, D. D., and Shupe, M. D.: Cloud property estimates from zenith spectral measurements of scattered sunlight between 0.9 and 1.7 μm, J. Geophys. Res., 111, D16208, doi:10.1029/2005JD006641, 2006. 5295

Evans, K. F.: The spherical harmonics discrete ordinate method for three-dimensional atmospheric radiative transfer, J. Atmos. Sci., 55, 429–446, doi:10.1175/1520-0469(1998)055<0429:TSHDOM>2.0.CO;2, 1998. 5301

Hu, Y., Wielicki, B., Lin, B., Gibson, G., Tsay, S.-C., Stamnes, K., and Wong, T.: δ-fit: a fast and accurate treatment of particle scattering phase functions with weighted singular-value decomposition least-squares fitting, J. Quant. Spectrosc. Ra., 65, 681–690, 2000. 5301

Iwabuchi, H. and Hayasaka, T.: Effects of cloud horizontal inhomogeneity on the optical thickness retrieved from moderate-resolution satellite data, J. Atmos. Sci., 59, 2227–2242, 2002. 5319

Key, J. R. and Intrieri, J. M.: Cloud particle phase determination with the AVHRR, J. Appl. Meteorol., 39, 1797–1804, doi:10.1175/1520-0450-39.10.1797, 2000. 5294

Title Page

Abstract | Introduction

Conclusions | References

Tables | Figures

|◄ | ►|

◄ | ►

Back | Close

Full Screen / Esc

Printer-friendly Version

Interactive Discussion

Kikuchi, N., Nakajima, T., Kumagai, H., Kuroiwa, H., Kamei, A., Nakamura, R., and Naka-jima, T. Y.: Cloud optical thickness and effective particle radius derived from transmitted solar radiation measurements: comparison with cloud radar observations, J. Geophys. Res., 111, D07205, doi:10.1029/2005JD006363, 2006. 5295, 5296, 5314, 5315, 5319, 5323

Kindel, B. C., Schmidt, K. S., Pilewskie, P., Baum, B. A., Yang, P., and Platnick, S.: Obser-vations and modeling of ice cloud shortwave spectral albedo during the Tropical Compo-sition, Cloud and Climate Coupling Experiment (TC 4), J. Geophys. Res., 115, D00J18, doi:10.1029/2009JD013127, 2010. 5297

Kurucz, R. L.: Synthetic infrared-spectra, in: Infrared Solar Physics, edited by: Rabin, D. M., Jef-feries, J. T., and Lindsey, C., no. 154 in IAU SYMPOSIA, Int Astron Union, Kluwer Academic Publ, PO BOX 17, 3300 AA Dordrecht, the Netherlands, 523–531, 1994. 5301

LeBlanc, S. E., Schmidt, K. S., Pilewskie, P., Redemann, J., Hostetler, C., Ferrare, R., Hair, J., Langridge, J. M., and Lack, D. A.: Spectral aerosol direct radiative forcing from airborne radiative measurements during CalNex and ARCTAS, J. Geophys. Res., 117, D00V20, doi:10.1029/2012JD018106, 2012. 5297

Marshak, A., Knyazikhin, Y., Evans, K. D., and Wiscombe, W. J.: The "RED versus NIR" plane to retrieve broken-cloud optical depth from ground-based measurements, J. Atmos. Sci., 61, 1911–1925, 2004. 5295

Marshak, A., Platnick, S., Várnai, T., Wen, G., and Cahalan, R. F.: Impact of three-dimensional radiative effects on satellite retrievals of cloud droplet sizes, J. Geophys. Res., 111, D09207, doi:10.1029/2005JD006686, 2006. 5319

Mayer, B. and Kylling, A.: Technical note: The libRadtran software package for radiative trans-fer calculations - description and examples of use, Atmos. Chem. Phys., 5, 1855–1877, doi:10.5194/acp-5-1855-2005, 2005. 5301

McBride, P. J., Schmidt, K. S., Pilewskie, P., Kittelman, A. S., and Wolfe, D. E.: A spectral method for retrieving cloud optical thickness and effective radius from surface-based transmittance measurements, Atmos. Chem. Phys., 11, 7235–7252, doi:10.5194/acp-11-7235-2011, 2011. 5295, 5296, 5297, 5311, 5314, 5315, 5316, 5318, 5320, 5322, 5323, 5332

McBride, P. J., Schmidt, K. S., Pilewskie, P., Walther, A., Heidinger, A. K., Wolfe, D. E., Fairall, C. W., and Lance, S.: CalNex cloud properties retrieved from a ship-based spec-trometer and comparisons with satellite and aircraft retrieved cloud properties, J. Geophys. Res.-Atmos., 117, 1–10, doi:10.1029/2012JD017624, 2012. 5295

Cloud property retrieval using transmitted spectra

S. E. LeBlanc et al.

Title Page

Abstract	Introduction
Conclusions	References
Tables	Figures

Back | Close

Full Screen / Esc

Printer-friendly Version

Interactive Discussion

Discussion Paper | Discussion Paper | Discussion Paper | Discussion Paper

Michalsky, J., Min, Q., Barnard, J., Marchand, R., and Pilewskie, P.: Simultaneous spectral albedo measurements near the Atmospheric Radiation Measurement Southern Great Plains (ARM SGP) central facility, J. Geophys. Res., 108, 4254, doi:10.1029/2002JD002906, 2003. 5302, 5336

Minnis, P., Kratz, D. P., Coakley Jr., J. A., King, M. D., Garber, D., Heck, P., Mayor, S., Young, D. F., and Arduini, R.: Cloud Optical Property Retrieval (Subsystem 4.3), Clouds and the Earth's Radiant Energy System (CERES) Algorithm Theoretical Basis Document, 3, 135–176, 1995. 5299, 5300

Nakajima, T. and King, M. D.: Determinination of the optical thickness and effective particle radius of clouds from reflected solar radiation measurements. Part I: Theory, J. Atmos. Sci., 47, 1878–1893, doi:10.1175/1520-0469(1990)047<1878:DOTOTA>2.0.CO;2, 1990. 5295, 5314, 5323

Nakajima, T. and Tanaka, M.: Algorithms for radiative intensity calculations in moderately thick atmospheres using a truncation approximation, J. Quant. Spectrosc. Ra., 40, 51–69, 1988. 5301

Pilewskie, P. and Twomey, S.: Discrimination of ice from water in clouds by optical remote sensing, Atmos. Res., 21, 113–122, 1987. 5295, 5300

Pilewskie, P., Pommier, J., Bergstrom, R., Gore, W., Howard, S., Rabbette, M., Schmid, B., Hobbs, P. V., and Tsay, S. C.: Solar spectral radiative forcing during the Southern African regional science initiative, J. Geophys. Res., 108, 1–7, doi:10.1029/2002JD002411, 2003. 5297

Platnick, S.: Vertical photon transport in cloud remote sensing problems, J. Geophys. Res., 105, 22919–22935, 2000. 5295, 5319, 5323

Platnick, S., Li, J. Y., King, M. D., Gerber, H., and Hobbs, P. V.: A solar reflectance method for retrieving the optical thickness and droplet size of liquid water clouds over snow and ice surfaces, J. Geophys. Res., 106, 15185–15199, 2001. 5295

Platnick, S., King, M. D., Ackerman, S. A., Menzel, W. P., Baum, B. A., Riedi, J. C., and Frey, R. A.: The MODIS cloud products: algorithms and examples from Terra, IEEE T. Geosci. Remote, 41, 459–473, 2003. 5299, 5318

Ptashnik, I. V., Smith, K. M., Shine, K. P., and Newnham, D. A.: Laboratory measurements of water vapour continuum absorption in spectral region 5000–5600 cm^{-1}: evidence for water dimers, Q. J. Roy. Meteor. Soc., 130, 2391–2408, doi:10.1256/qj.03.178, 2004. 5337

Cloud property retrieval using transmitted spectra

S. E. LeBlanc et al.

Title Page

Abstract | Introduction

Conclusions | References

Tables | Figures

◀ | ▶

◀ | ▶

Back | Close

Full Screen / Esc

Printer-friendly Version

Interactive Discussion

Rawlins, F. and Foot, J.: Remotely sensed measurements of stratocumulus properties during FIRE using the C130 aircraft multi-channel radiometer., J. Atmos. Sci., 47, 2488–2504, 1990. 5295, 5296

Ricchiazzi, P., Yang, S., Gautier, C., and Sowle, D.: SBDART: a research and teaching software tool for plane-parallel radiative transfer in the Earth's atmosphere, B. Am. Meteorol. Soc., 79, 2101–2114, doi:10.1175/1520-0477(1998)079<2101:SARATS>2.0.CO;2, 1998. 5301

Rothman, L. S., Gordon, I. E., Barbe, A., Benner, D. C., Bernath, P. F., Birk, M., Boudon, V., Brown, L. R., Campargue, A., and Champion, J. P.: The HITRAN 2008 molecular spectroscopic database, J. Quant. Spectrosc. Ra., 110, 533–572, doi:10.1016/j.jqsrt.2009.02.013, 2009. 5337

Schaaf, C. B., Gao, F., Strahler, A. H., Lucht, W., Li, X., Tsang, T., Strugnell, N. C., Zhang, X., Jin, Y., Muller, J.-P., Lewis, P., Barnsley, M., Hobson, P., Disney, M., Roberts, G., Dunderdale, M., Doll, C., D'Entremont, R. P., Hu, B., Liang, S., Privette, J. L., and Roy, D.: First operational BRDF, albedo nadir reflectance products from MODIS, Remote Sens. Environ., 83, 135–148, doi:10.1016/S0034-4257(02)00091-3, 2002. 5299, 5336

Schofield, R., Daniel, J. S., Portmann, R. W., Miller, H. L., Solomon, S., Eubank, C. S., Melamed, M. L., Langford, A. O., Shupe, M. D., and Turner, D. D.: Retrieval of effective radius and liquid water path from ground-based instruments: a case study at Barrow, Alaska, J. Geophys. Res., 112, D21203, doi:10.1029/2007JD008737, 2007. 5295

Slingo, A.: Sensitivity of the Earth's radiation budget to changes in low clouds, Nature, 343, 49–51, 1990. 5294

Stamnes, K., Tsay, S., Wiscombe, W. J., and Laszlo, I.: DISORT, a general-purpose Fortran program for discrete-ordinate-method radiative transfer in scattering and emitting layered media: documentation of methodology, Tech. rep., Dept. of Physics and Engineering Physic, Stevens Institute of Technology, Hoboken, NJ 07030, 2000. 5301

Sun, Z. and Shine, K. P.: Studies of the radiative properties of ice and mixed-phase clouds, Q. J. Roy. Meteor. Soc., 120, 111–137, 1994. 5319

Sun, Z. and Shine, K. P.: Parameterization of ice cloud radiative properties and its application to the potential climatic importance of mixed-phase clouds, J. Climate, 8, 1874–1888, 1995. 5294

Taylor, J. R.: An introduction to error analysis: the study of uncertainties in physical measurements, University Science Books, 1997. 5314

Cloud property retrieval using transmitted spectra

S. E. LeBlanc et al.

Title Page

Abstract	Introduction
Conclusions	References
Tables	Figures

|◀ | ▶|

◀ | ▶

Back | Close

Full Screen / Esc

Printer-friendly Version

Interactive Discussion

Turner, D. D., Vogelmann, A. M., Johnson, K., Miller, M., Austin, R. T., Barnard, J. C., Flynn, C., Long, C., McFarlane, S. A., Cady-Pereira, K., Clough, S. A., Chiu, J. C., Khaiyer, M. M., Liljegren, J., Lin, B., Minnis, P., Marshak, A., Matrosov, S. Y., Min, Q., O'Hirok, W., Wang, Z., and Wiscombe, W.: Thin liquid water clouds: their importance and our challenge, B. Am. Meteorol. Soc., 88, 177–190, doi:10.1175/BAMS-88-2-177, 2007. 5295

Twomey, S. and Bohren, C. F.: Simple approximations for calculations of absorption in clouds, J. Atmos. Sci., 37, 2086–2095, doi:10.1175/1520-0469(1980)037<2086:SAFCOA>2.0.CO;2, 1980. 5294

Twomey, S. and Cocks, T.: Remote sensing of cloud parameters from spectral reflectance in the near-infrared, Beiträge zur Physik der Atmosphäre, 62, 172–179, 1989. 5295

Vukicevic, T., Coddington, O., and Pilewskie, P.: Characterizing the retrieval of cloud properties from optical remote sensing, J. Geophys. Res., 115, 1–14, doi:10.1029/2009JD012830, 2010. 5296, 5324

Wan, Z. and Li, Z.-l.: A physics-based algorithm for retrieving land-surface emissivity and temperature from EOS/MODIS data, IEEE T. Geosci. Remote, 35, 980–996, 1997. 5312

Warren, S. G. and Brandt, R. E.: Optical constants of ice from the ultraviolet to the microwave: a revised compilation, J. Geophys. Res., 113, 1–10, doi:10.1029/2007JD009744, 2008. 5337

Wiscombe, W.: Improved Mie scattering algorithms, Appl. Optics, 19, 1505–1509, 1980. 5301, 5337

Wiscombe, W. and Warren, S.: A model for the spectral albedo of snow. I: Pure snow, J. Atmos. Sci., 37, 2712–2733, doi:10.1175/1520-0469(1980)037<2712:AMFTSA>2.0.CO;2, 1980. 5302

Wiscombe, W. J., Welch, R. M., and Hall, W. D.: The effects of very large drops on cloud absorption. Part I: Parcel models, J. Atmos. Sci., 41, 1336–1355, doi:10.1175/1520-0469(1984)041<1336:TEOVLD>2.0.CO;2, 1984. 5294

Zhang, S., Xue, H., and Feingold, G.: Vertical profiles of droplet effective radius in shallow convective clouds, Atmos. Chem. Phys., 11, 4633–4644, doi:10.5194/acp-11-4633-2011, 2011. 5319

Cloud property retrieval using transmitted spectra

S. E. LeBlanc et al.

Title Page

Abstract	Introduction
Conclusions	References
Tables	Figures

|◄ | ►|

◄ | ►

Back | Close

Full Screen / Esc

Printer-friendly Version

Interactive Discussion

Table 1. Definition, wavelength range used, and expected behavior for the 15 spectral parameters. L_λ indicates the radiance evaluated at a wavelength, λ, in microns. The function $\lin(y; \lambda = a.b)$ describes the linear fit of values evaluated at $\lambda = a$ and $\lambda = b$, where represents any variable that is calculated from the radiance spectrum. The function $m(y)|_{\lambda=a}^{b}$ describes the slope of y evaluated over the range of $\lambda = a$ to $\lambda = b$. The average value of y over the range of $\lambda = a$ to $\lambda = b$ is presented as $\langle y \rangle|_{\lambda=a}^{b}$. In addition to defining each spectral parameter by the symbol η_1 through η_{15}, other symbols are used to provide additional insight in the calculation of the parameter. For parameters defined by a measure of the curvature of radiance, C_λ is used, where a convex curvature represents a slope that decreases with increasing wavelength, and concave curvature for a slope that increases with increasing wavelength. The spectral derivatives of the normalized radiances are denoted by $\frac{\partial}{\partial \lambda_\lambda}$. When this derivative, as a function of wavelength, is fitted to a line, its slope is represented by $\frac{\partial^2}{\partial \lambda_\lambda^2}$. The slope of this derivative over a wavelength range is roughly equivalent to the average second derivative over the same wavelength range, but differences may result from the linear fitting process. Slopes, ratios, mean, and normalized radiances are presented as sl_λ, r_λ, $\langle R \rangle_\lambda$, and R_λ respectively, with λ denoting a representative wavelength in microns where the features are quantified.

	Wavelength(s) (nm)	Calculation	Method	Units	Description and expected behavior
η_1	1000–1100	$C_{1.0} = \sum\limits_{\lambda=1.0}^{1.1} \left[\frac{L(\lambda)}{L_{1.0}} - \lin\left(\frac{L(\lambda)}{L_{1.0}}\right)\Big|_{\lambda=1.0}^{1.1} \right]$	Curvature	–	At $\tau > 30$, the curvature is positive for liquid clouds, and negative for ice clouds. Separation between ice and liquid clouds is larger for larger r_e. Positive values represent a convex shape, while negative values represent a concave shape.
η_2	1200	$\frac{\partial}{\partial \lambda_{1.2}} = \frac{\partial}{\partial \lambda} \frac{L_{1.2}}{L_{1.0}}$	Derivative	μm^{-1}	Not dependent on τ and r_e for liquid clouds, but becomes more negative for ice clouds as τ and r_e are increased.
η_3	1500	$\frac{\partial}{\partial \lambda_{1.5}} = \frac{\partial}{\partial \lambda} \frac{L_{1.5}}{L_{1.0}}$	Derivative	μm^{-1}	Sensitive to differences in ice and liquid cloud with $\tau < 10$. η_3 decreases as r_e decreases and τ increases.

Table 1. Continued.

	Wavelength(s) (nm)	Calculation	Method	Units	Description and expected behavior
η_4	1200 &1237	$r_{1.2} = \frac{L_{1.2}}{L_{1.237}}$	Ratio	–	Dependent on τ and r_e for ice cloud especially for $\tau > 30$, but not for liquid cloud. Increases with increasing of ice clouds.
η_5	1245–1270	$\langle R \rangle_{1.25} = \left\langle \frac{L(\lambda)}{L_{max}} \right\rangle \Big\vert_{\lambda=1.245}^{1.27}$	Mean	–	Dependent on cloud water content independent of ϕ. Decreases with increasing water content.
η_6	1565–1640	$\langle R \rangle_{1.6} = \left\langle \frac{L(\lambda)}{L_{max}} \right\rangle \Big\vert_{\lambda=1.565}^{1.64}$	Mean	–	Dependent on τ, r_e, and ϕ for $\tau < 30$. Decreases with increasing τ. Larger decrease for ice cloud than liquid cloud.
η_7	1000–1050	$\langle R \rangle_{1.0} = \left\langle \frac{L(\lambda)}{L_{max}} \right\rangle \Big\vert_{\lambda=1.0}^{1.05}$	Mean	–	Dependent on cloud water content, with only small variation due to ϕ as compared to variations due to τ. Decreases with increasing water content for ice cloud $\tau > 10$, and liquid cloud $\tau > 20$.
η_8	1490–1600	$C_{1.6} = \sum\limits_{\lambda=1.49}^{1.6} \left(\frac{L(\lambda)}{L_{1.0}} - \mathrm{lin}\left(\frac{L(\lambda)}{L_{1.0}} \Big\vert_{\lambda=1.49}^{1.6} \right) \right)$	Curvature	–	Decreases with increasing τ. Clear separation between ice and liquid cloud, and r_e at $\tau < 30$. Positive values represent a convex shape, while negative values represent a concave shape.
η_9	1000–1080	$\frac{\partial^2}{\partial \lambda_{1.0}^2} = m\left(\frac{\partial}{\partial \lambda} \frac{L(\lambda)}{L_{1.0}} \Big\vert_{\lambda=1.0}^{1.08} \right)$	Slope of derivative	$\mu m^{-1} nm^{-1}$	Increases with increasing ice cloud τ, but decreases with increasing liquid cloud τ. These changes are amplified as r_e increases. Positive values only for ice cloud.

Table 1. Continued.

	Wavelength(s) (nm)	Calculation	Method	Units	Description and expected behavior
η_{10}	1200–1310	$\frac{\partial^2}{\partial \lambda_{1.2}^2} = m\left(\frac{\partial}{\partial \lambda} \frac{L(\lambda)}{L_{1.0}}\bigg|_{\lambda=1.2}^{1.31}\right)$	Slope of derivative	$\mu m^{-1}\,nm^{-1}$	Only ice clouds produce positive values. Increases with increasing ice cloud τ, and decreases with τ in liquid clouds for $\tau < 50$.
η_{11}	530–610	$sl_{0.55} = m\left(\frac{L(\lambda)}{L_{max}}\bigg|_{\lambda=0.53}^{0.61}\right)$	Slope	μm^{-1}	Largest gradient due to τ occurs at $\tau < 4$. Dependence on r_e and solar zenith angle for $\tau > 10$.
η_{12}	1040	$R_{1.04} = \frac{L_{1.04}}{L_{max}}$	Normalized radiance	–	Smaller variations due to r_e than η_7. Decreases with decreasing τ for clouds of $\tau > 20$.
η_{13}	1000 & 1065	$r_{1.0} = \frac{L_{1.0}}{L_{1.065}}$	Ratio	–	Decreases with increasing liquid cloud τ and r_e. Increases with increase in ice cloud τ.
η_{14}	600 & 870	$r_{0.6} = \frac{L_{0.6}}{L_{0.87}}$	Ratio	–	Most sensitive to τ for clouds with $\tau < 20$. Little variation due to liquid r_e compared to variations due to τ. Larger variations due to ice r_e than τ.
η_{15}	1565–1634	$sl_{1.6} = m\left(\frac{L(\lambda)}{L_{1.565}}\bigg|_{\lambda=1.565}^{1.634}\right)$	Slope	μm^{-1}	Increases with increase in τ and r_e. Larger increase for ice clouds than for liquid clouds same parameter introduced by McBride et al. (2011) but calculated from normalized radiance and not transmittance.

Table 2. Root-mean-square (rms) of the percent difference for the entire wavelength range between modeled spectra based on the 3 different retrievals and the 3 sample measured spectra presented in Fig. 13.

	Current Work (%)	Slope (%)	2-wavelength (%)
Case A	3.1	6.4	5.9
Case B	7.2 (22.8 for ice)	13.3	7.3
Case C	5.9	22.5	20.2

Full Screen / Esc

Printer-friendly Version

Interactive Discussion
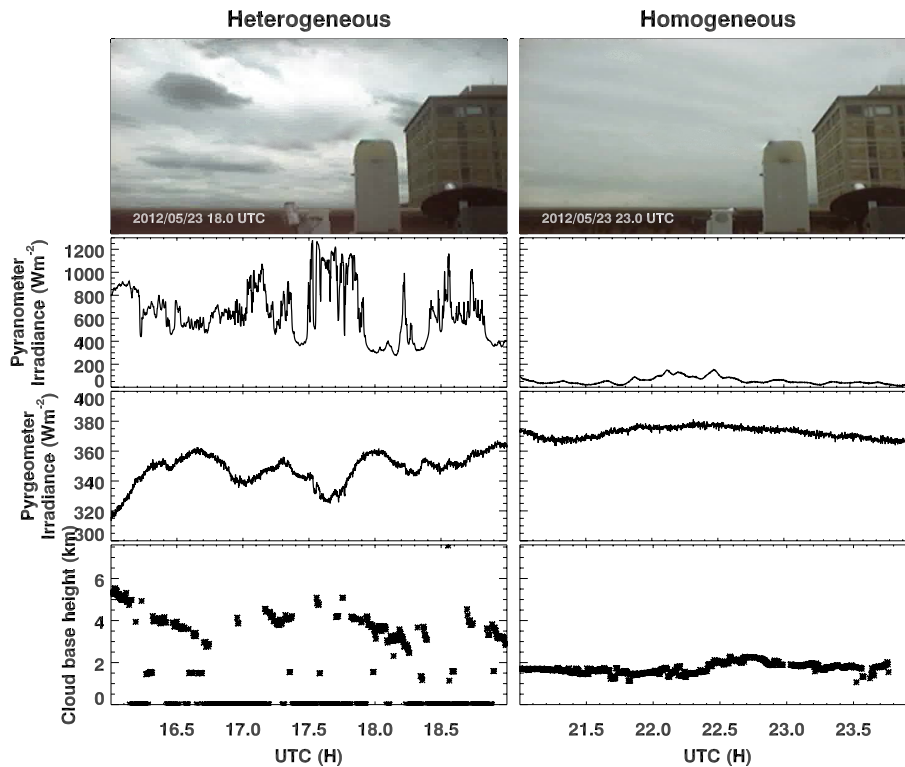
Figure 1. Broadband short- (pyranometer) and long-wave (pyrgeometer) irradiance and cloud base heights (ceilometer) for horizontally heterogeneous (left panel) and homogeneous (right panel) clouds taken on 23 May 2012. The top panel presents one image from the sky web cam for either heterogeneous or homogeneous clouds taken from the Skywatch observatory.
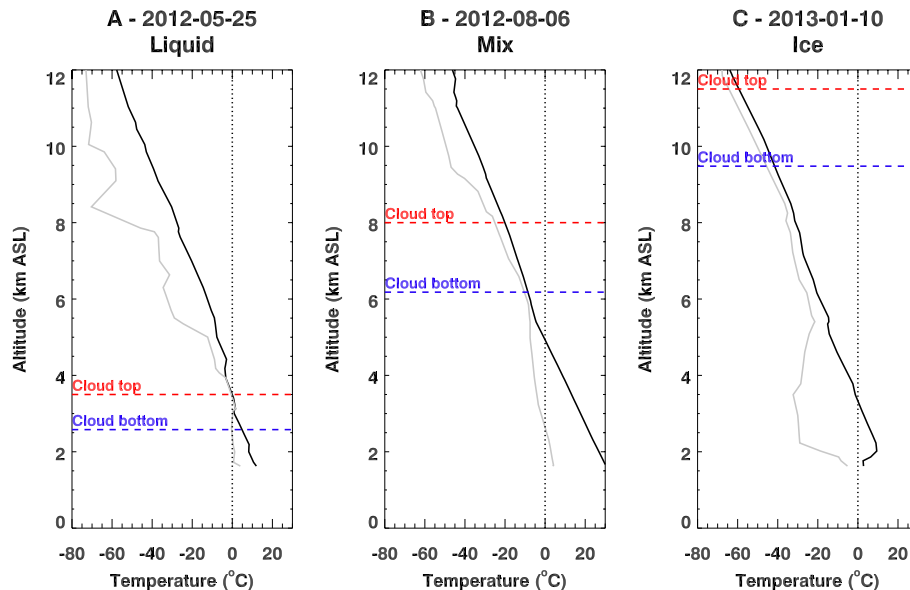
Figure 2. Atmospheric sounding profiles of temperature (black) and dew point (grey) taken near Denver International Airport for the case study time periods: **(A)** liquid cloud case on 25 May 2012, **(B)** mixed-phase cloud case on 6 August 2012, and **(C)** ice cloud case on 10 January 2013. Cloud bottom and top values determined from ground-based and satellite data (see text).
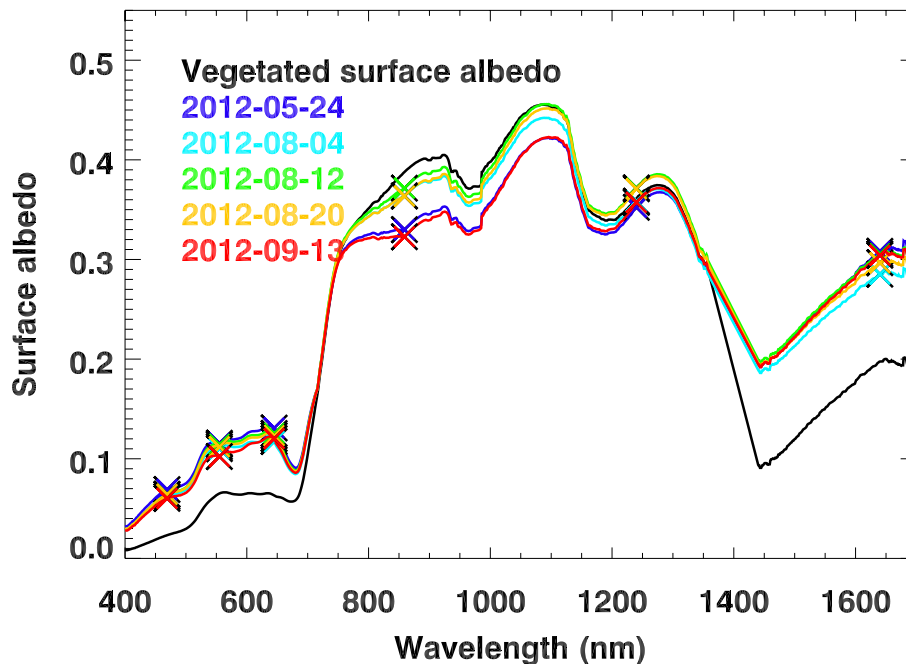
Figure 3. Spectral surface albedo used as input for the radiative transfer modeling for spring/summer. To approximate a full spectrum for varying days, the vegetated spectral surface albedo (black line) measured by Michalsky et al. (2003) is scaled using the discrete-band surface albedo product retrieved from Moderate Resolution Imaging Spectroradiometer (MODIS) measurements (Schaaf et al., 2002) at the wavelengths denoted by "X". This scaling is interpolated between the discrete MODIS bands.
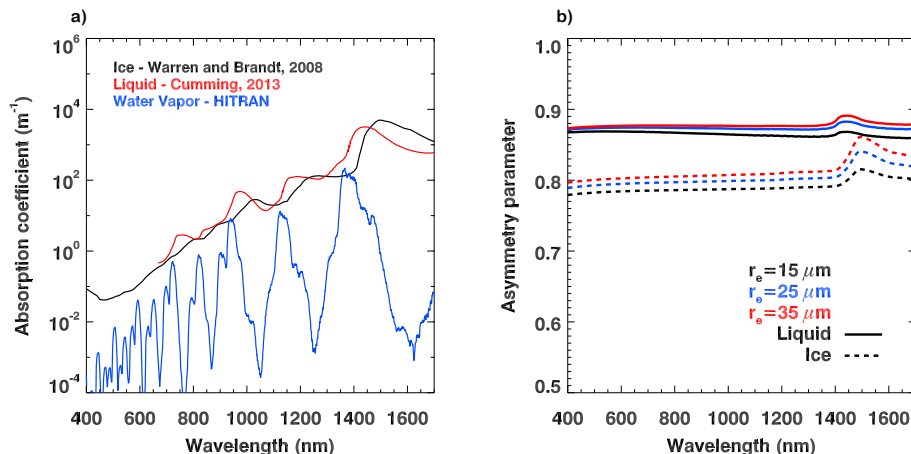
Figure 4. (a) Spectral bulk absorption coefficient and **(b)** asymmetry parameter for different thermodynamic phases of water. Notice the local maxima offset between ice water, liquid water, and water vapor near 900 nm, 1100 nm, and 1400 nm. The bulk ice absorption coefficient has been determined by Warren and Brandt (2008), while the bulk liquid water absorption coefficient has been determined by Cumming (2013). The bulk water vapor absorption has been calculated using the HITRAN model described by Rothman et al. (2009) for an optical path length of 10 m with pure water vapor pressure of 15 hPa at 293 K (Ptashnik et al., 2004). The asymmetry parameter for liquid drops were calculated from Mie scattering calculation following the methodology developed by Wiscombe (1980). Ice asymmetry parameter were obtained from the scattering models for severely roughened general habit mixture described by Baum et al. (2011).

Title Page

Abstract   Introduction

Conclusions   References

Tables   Figures

|◄   ►|

◄   ►

Back   Close

Full Screen / Esc

Printer-friendly Version

Interactive Discussion
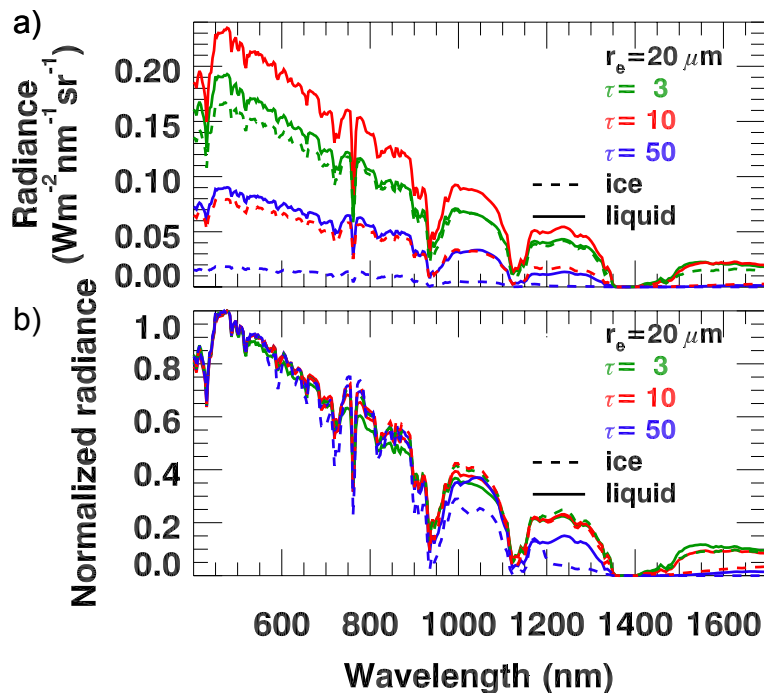
Figure 5. Modeled zenith radiance spectra transmitted through clouds with a few combinations of optical thickness (τ) for ice and liquid water clouds with an effective radius (r_e) of 20 µm for the atmospheric state and surface albedo defined for 25 May 2012 and a solar zenith angle of 50°. Top panel **(a)** shows the radiance spectra in $W\,m^{-2}\,nm^{-1}\,sr^{-1}$ units and bottom panel **(b)** shows the radiance spectra normalized by their maximum value (unitless). The radiance minima centered at 760 nm, 940 nm, 1130 nm, and 1400 nm represent gas absorption bands that are ignored in this work.
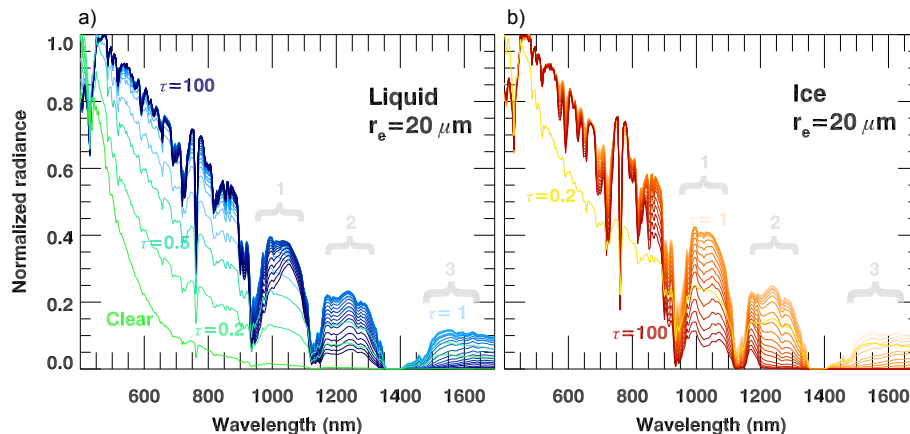
Figure 6. Normalized radiance spectra for liquid (left) and ice (right) clouds with an r_e of 20 µm and τ varying from 0.2 to 100 (where darker colors denotes optically thicker clouds). A clear sky normalized radiance (denoted in green) is added for comparison to the optically thinnest clouds. Three wavelength ranges where there are spectral features are indicated by the grey curly brackets.

Full Screen / Esc
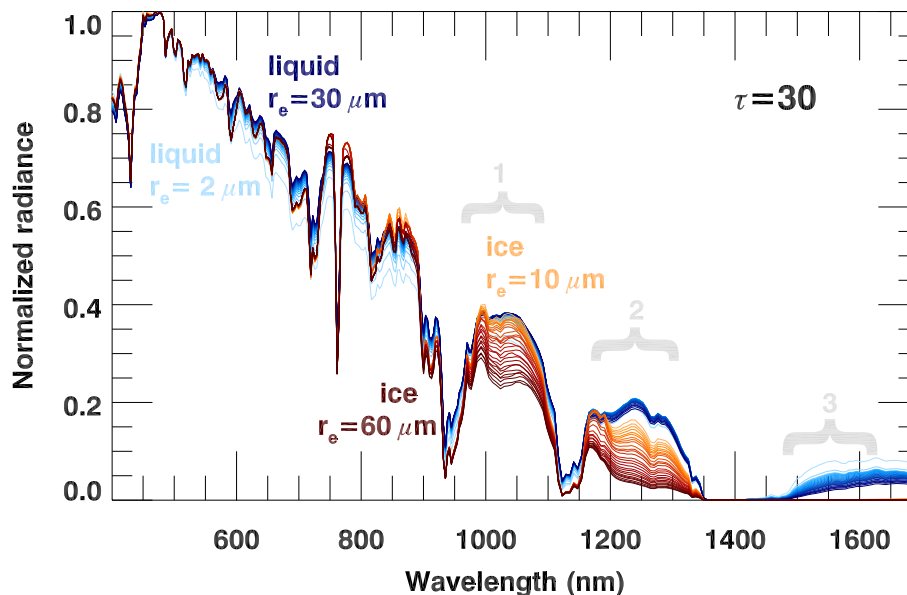
Figure 7. Normalized radiance spectra transmitted through liquid and ice clouds of τ of 30 and r_e ranging from 2 μm to 30 μm for liquid clouds and 10 μm to 60 μm for ice clouds. Darker orange lines represent radiance spectra transmitted through larger ice particles. Darker blue lines represent the radiance spectra transmitted through larger liquid cloud droplets. 3 wavelength ranges where there are spectral features are indicated by the grey curly brackets.
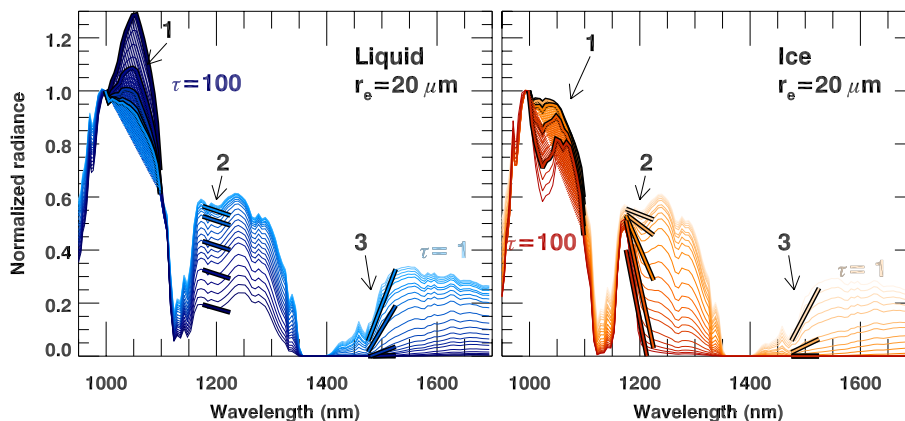
Figure 8. Radiance spectra normalized by its value at 1000 nm for liquid (left) and ice (right) clouds with $r_e = 20\,\mu$m and τ varying from 1 to 100 (where darker colors denotes optically thicker clouds). Three spectral features, which vary with changes of τ, (see text) are quantified by the first 3 parameters, η_1, η_2, and η_3. The transmittance that contribute to calculating η_1, η_2, and η_3 are highlighted with a thicker line for a few transmittance spectra with varying τ and are indicated by the numbers "1", "2", and "3" respectively. The shaded areas indicated by "1" overlap for different optical thickness. To increase visibility of the smaller shaded areas (denoted by lighter blues and darker oranges), these are plotted in front of the larger shaded areas.
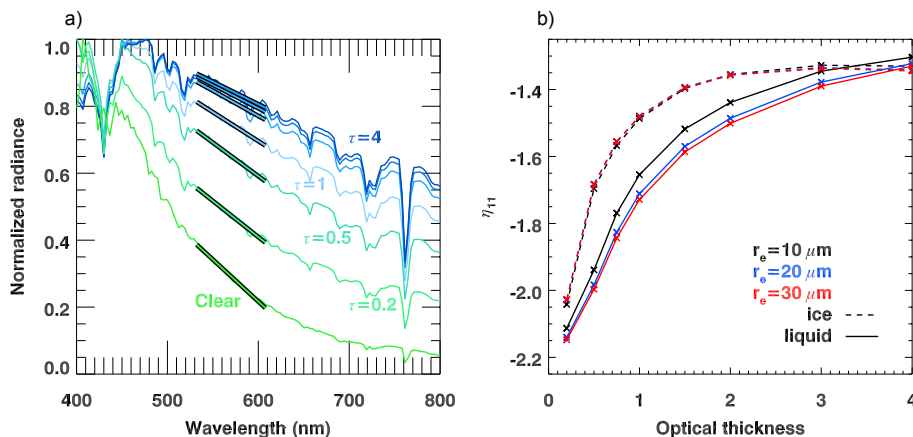
Figure 9. (a) Transmittance of liquid water clouds of varying optical thickness and effective radius of 20 µm and **(b)** the slope of normalized radiance for the wavelength range in 530–610 nm, η_{11}, as a function of τ for ice and liquid clouds, evaluated for 3 different effective radii. In **(a)**, the slope in the visible is identified by the highlighted region. The normalized radiance spectra and the η_{11} calculated from them were modeled with ancillary inputs based on 25 May 2012, for a solar zenith angle of 50°.

Cloud property retrieval using transmitted spectra

S. E. LeBlanc et al.
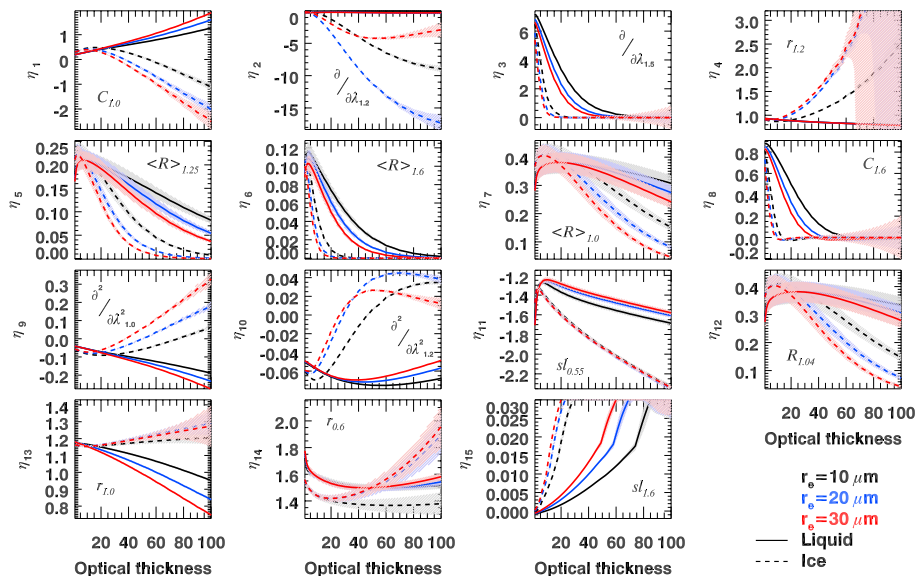
Figure 10. The value of the parameters, η_1 through η_{15}, as a function of optical thickness for 3 effective radii (colors) for liquid (solid) and ice (dashed) clouds. The shading surrounding each line denotes the standard deviation of the variability in the parameters due to measurement uncertainty (see text).
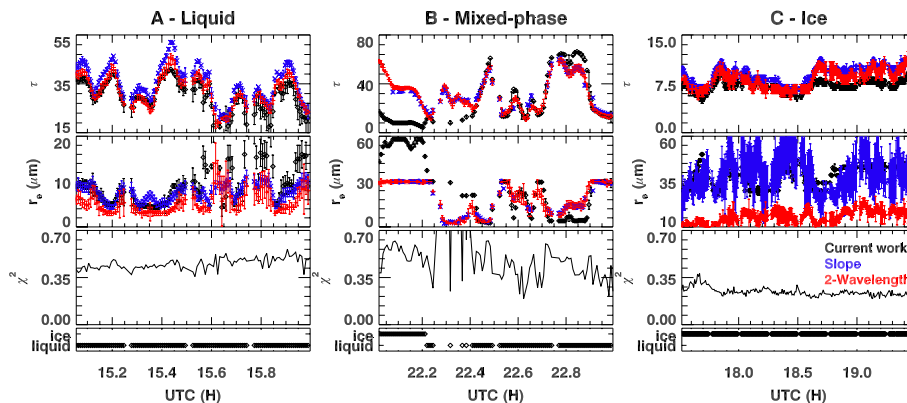
Figure 11. Time series of retrieved cloud properties determined by 3 different transmittance based retrieval methods; case A (left) for liquid cloud, case B (center) for mixed-phase cloud, and case C (right) for ice cloud. The mixed-phase cloud case represents a cloud sampled during a time where both ice and liquid water cloud particles are expected to have been present. Colors represent three different cloud retrieval methods: this work (black), the slope method (blue) and the 2-wavelength method (red). For each case study, the top-most panel presents the retrieved optical thickness, τ, the panel directly below shows the effective radius, r_e, the panel directly below shows the minimum χ^2 determined by this work (15-parameter method), and the lowest panel shows thermodynamic phase, ϕ, designated by this work. The y-axis scale in τ and r_e differs for each case.

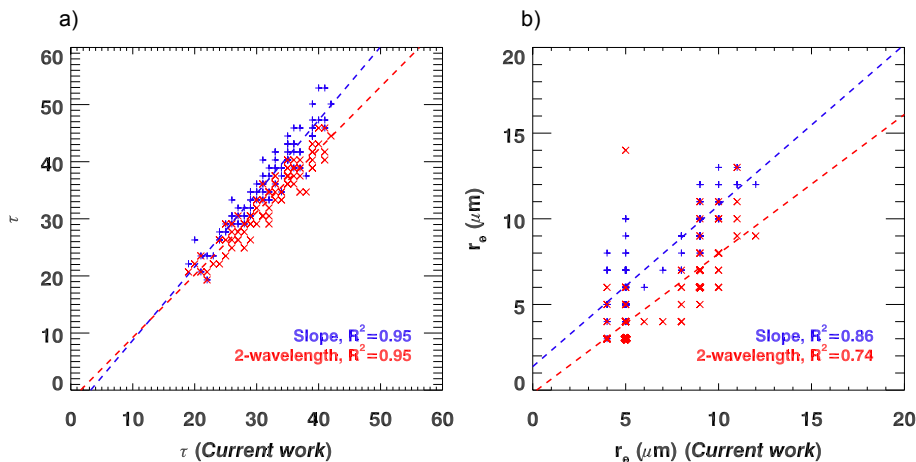**Figure 12.** Scatter plot of **(a)** optical thickness and **(b)** effective radius for the liquid water cloud (case A) from the slope (blue) and 2-wavelength (red) methods compared to the current work's retrieval. Dashed lines represent the best-fit lines. Larger thickness of the symbols indicates higher density of the points at that location.
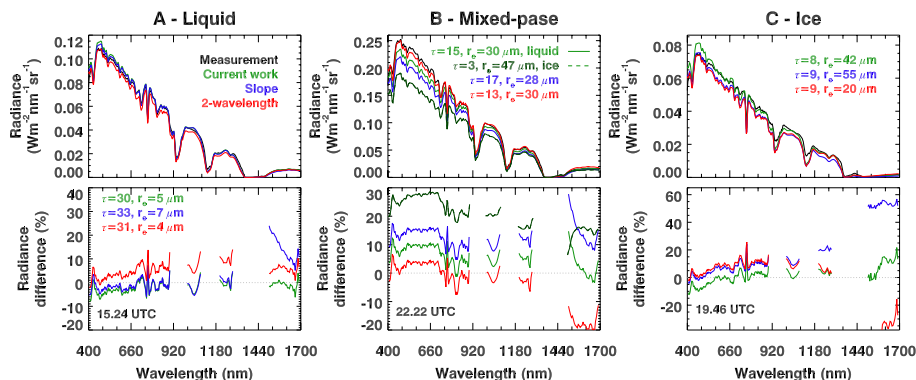
Figure 13. Sample measured and modeled spectra for the 3 different cloud case studies. Measured radiance spectra (black) are specific to a certain point (see legend) in the time series of Fig. 11. Modeled radiance spectra are based on the retrieved cloud properties from each method (this work = green; slope = blue, and 2-wavelength = red) for the same time instance. The percentage difference in the modeled spectra with respect to the measured spectra is shown in lower panels for wavelength regions outside of water vapor absorption bands. Modeled radiance spectra based on the current work's retrieval for an ice cloud (dashed line) and if it were a liquid cloud (solid line) is presented in case B. The slope and 2-wavelength modeled spectra represent a liquid cloud in case B.